

C 6 Theory of Scanning Tunneling Microscopy¹

S. Lounis

Peter Grünberg Institut & Institute for Advanced
Simulation

Forschungszentrum Jülich GmbH

Contents

1	Introduction	2
2	Description of scanning tunneling microscopy	3
3	The concept of tunneling	5
4	Modeling currents	7
4.1	Bardeen's approach	7
4.2	Tersoff-Hamann model	14
4.3	Different STM modes	17
4.4	Spin-polarization and tunneling: SP-STM and TAMR-STM	19
4.5	Crystal surfaces: $k_{ }$ -Selection in STM	25
5	Examples of simulations and experiments	27
5.1	Seeing the Fermi surface in real space via the induced charge oscillations . . .	27
5.2	Magnetism on surfaces with SP-STM	31
5.3	Magnetic domain walls with TAMR-STM	32

¹Lecture Notes of the 45th IFF Spring School “Computing Solids - Models, ab initio methods and supercomputing” (Forschungszentrum Jülich, 2014).

1 Introduction

Scanning tunneling microscopy (STM) is a tool that profoundly shaped nanoscience and nanotechnology. Since its invention by Rohrer and Binnig [1, 2, 3], for which they were awarded the 1986 Nobel prize in Physics, STM experienced revolutionary developments allowing to see for the first time nanostructures at the atomic scale. Another one is to access spintronics at the nanolevel. With increasing availability of low-temperature STM, local electronic properties can be investigated with unprecedented space and energy resolution which opens the vista to completely new applications. STM allowed the rather unique ability of accessing at the same time occupied and unoccupied electronic states. In Fig. 1 is shown a schematic view of the chronological achievements of STM during the last 20 years. Although one cannot mention all important milestones in a single figure, Fig. 1 tells us that after the initial application of STM as a visualization tool of substrates at the atomic level (surface topography), it developed quickly into a device for the manipulation of atoms. Indeed in the 90's, nanostructures such as corrals were built atom by atom whereby a fundamental quantum property, Friedel oscillations induced by the presence of impurities in an electron gas, were observed and confined within man-made nano-objects [4, 5, 6, 7]. These achievements were the prelude to functionalization of nanostructures for different applications, with the aim of characterizing and manipulating not only the spin and charge of single atoms or single molecules but also their position in much bigger nanostructures.

At the beginning of the 21st century, spin-polarized STM (SP-STM) was invented [8, 9] and applied for the investigation of magnetic layers on different substrates. It was, for example, found that a manganese monolayer deposited on tungsten(110) substrate is characterized by an antiferromagnetic ground state, confirming previous predictions made with first-principles calculations [10], and it was nicely shown that contrary to the regular STM, the spin-polarized version shows a magnetic superstructure on top of the chemical unit-cell. Magnetic characterization is nowadays a routine work, that allowed the discovery of new magnetic states, for example chirality, induced by the existence of Dzyaloshinskii-Moriya interactions, was revealed in the magnetic contrast measured on a manganese layer deposited on W(110) surface [11] (See Chapter C 4 by S. Blügel). Moreover, magnetism of finite nanostructures, nanowires for instance, on magnetic surfaces was recently characterized. [12, 13]

Being the ubiquitous apparatus for nanoscience, the range of phenomena studied by STM is continuously growing. Besides surface topography, and the investigation of ground state properties of excitations, vibrational [14], magnetic [15, 16, 17, 18] or optical [19] properties, which allow chemical identification of atoms, and even measurement of their magnetic anisotropy energy is today a major topic studied with state-of-the-art machines. Recently, magnetometry measurements allowed to extract quantitative values for magnetic exchange interactions among adatoms separated by large distances! [20, 21] Also other applications and developments of STM are geared towards the measurements of adhesion and strength of individual chemical bonds, friction, studies of dielectric properties, contact charging, molecular manipulation and many other phenomena from the micrometer down to subnanometer scale. As Chen says in his book [22]: *It was often said that STM is to nanotechnology what the telescope was to astronomy. Yet STM is capable of manipulating the objects it observes, to build nanoscale structures never existed in Nature. No telescope is capable of bringing Mars and Venus together.*

The actual playground of STM experiments was initially covered mainly by theory. The advent of such an instrument urged the theoretical community for the development of new methods that allows the understanding and prediction of phenomena accessible with STM (see e.g. Refs. [23,

24, 25, 26, 27] or Refs. [28, 29, 30, 31, 32, 33, 34, 35] and many others). It is clear that this tool will continue to experience further evolutions and to play a pivotal role in further developments of nanosciences. Thus more challenges will be proposed to theoreticians. It is not a surprise if after 20 years from its inventions, several books and reviews were dedicated to this technique, to cite a few see Refs. [36, 37, 38, 39, 40, 41, 42, 43].

The goal of this lecture is to review the basics behind the theory accompanying the experiment which could be of interest for readers aiming to work in this field or for those who want to reassess some of the fundamental concepts. Several flavors of the STM method have been developed and invented, we cannot go over all of them but we will discuss the standard ones following partly the book of Chen [22] and the lecture notes of Stefan Blügel [44].

Chronological developments:

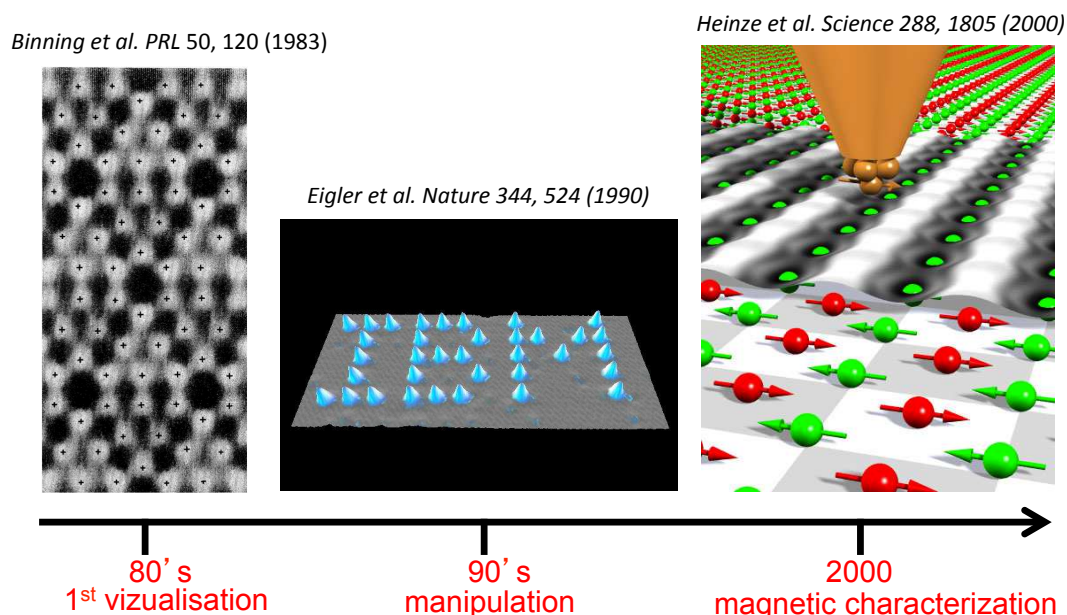


Fig. 1: Chronological developments of STM. At the early days of its invention, STM was used as a visualization tool for surface topography. It developed into a unique tool that allows access to occupied and unoccupied electronic states. Then atomic manipulation was achieved and magnetic contrasts were realized thanks to the spin-polarized STM. We note that it is impossible to mention all milestones that STM allowed to reach.

2 Description of scanning tunneling microscopy

Before discussing the basic theory explaining the measurements that can be done with STM, a description of this tool is needed. A crucial ingredient in any STM is the probe tip that is attached to a piezodrives, which consists of three mutually perpendicular piezoelectric transducers (x, y and z piezo). Upon applying a voltage, a piezoelectric transducers contracts or expands which allows to move the tip on the surface. Since the tip is not touching the substrate, the flowing current, I , is weak and is obtained via a tunneling mechanism through the vacuum.

Fig. 2(a) shows a schematic picture of an STM device. If a bias voltage, V , is applied between the tip and the sample, the tunneling current can change.

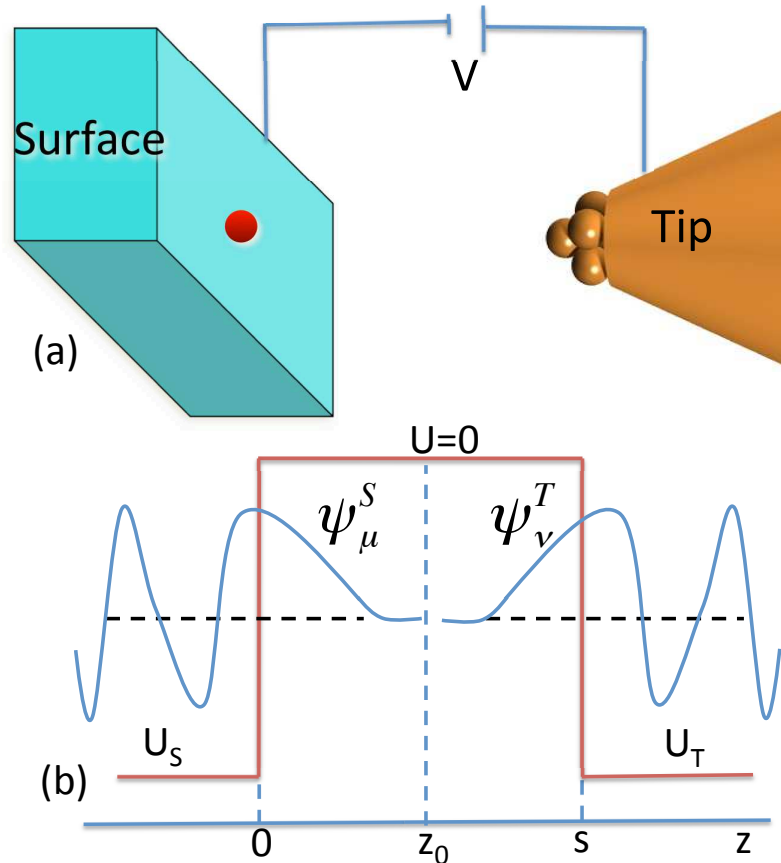


Fig. 2: A schematic picture of STM is shown in (a). A current can flow between the tip and the substrate through vacuum via a tunneling mechanism. In quantum mechanics, a particle has a non-zero probability of tunneling through a potential barrier which in the STM case is induced by the vacuum. A simple barrier as shown in (b) explains the physics of tunneling. When the two electrodes are far apart, the wave functions of both electrodes A and B decay into the vacuum while the tunneling can take place if the electrodes are closer.

The simplest way to obtain a scanning tunneling microscope image is to directly measure the variation of the tunnel current as a function of the scanning position while keeping the distance between tip and sample surface constant. A so-called current image is then obtained. Instead of directly recording the atomic variation of the current, however the usual procedure is to keep the tunnel current constant while scanning over the surface. This is done by changing the distance between the tip and surface using a feedback loop. In order to get an image, the voltage required at the piezoelectric crystal to adjust the distance is recorded. One obtains then the so-called constant-current STM image. A further operation mode is the spectroscopy acquisition by STM. It is usually done by interrupting the feedback in order to keep for the $I-V$ spectroscopy data acquisition the tip-sample separation constant. This can be done at any

desired surface spot or for every pixel in a STM image. An extended discussion of the different operating modes will be given once the theory of STM is presented.

Obviously, if one wants to understand the working mechanism of STM and simulate the experiment, one could think of simulating the whole setup, i.e. considering a tip, a substrate, a bias voltage and calculate the tunneling current or conductance (see e.g. Chapter **A 9** by S. Tsukamoto). Although actual ab-initio methods are capable of handling few hundreds up to few thousands of atoms in a unit-cell (see e.g. Chapter **D 6** by R. Zeller), technical issues can occur. For instance, a periodic supercell approach would lead to a non-realistic scenario of multiples tips scanning the substrate at the same time. Methods based on Green functions allow to consider two perfect semi-infinite substrates separated by vacuum. One of the substrates would simulate the surface, on the other substrate, a model tip can be embedded (see e.g. Ref. [45]). Although this scheme is appealing, one would be facing the problem of choosing the right model for the tip, which is far from being easily accessible experimentally. All of those arguments stimulated approximations that are very often used successfully for the understanding of STM-experiments but they also bear limitations.

3 The concept of tunneling

Here we describe briefly elementary theories of tunneling through a one-dimensional potential barrier, which will help us to grasp the basic concept used in STM. In quantum mechanics, the electron feeling a potential $U(z)$, for example the one shown in Fig. 2(b) considering $U_S = U_T = -U$, is described by a wave function $\psi(z)$, which satisfies the Schrödinger equation,

$$-\frac{\hbar^2}{2m} \frac{d^2}{dz^2} \psi(z) + U(z)\psi(z) = E\psi(z), \quad (1)$$

at a given position z . In this elementary model, the STM setup is simplified to a one-dimensional potential barrier where the vacuum is modeled by the potential barrier U , while its left and right sides shown in Fig. 2(b) represent the substrate, S , and the tip, T . When $E > |U|$, the solutions of Eq. 1 are $\psi(z) = \psi(0)e^{\pm ikz}$ where $k = \frac{\sqrt{2m(E-|U|)}}{\hbar}$ is the wave vector. In the classically forbidden region, within the barrier, the solution is given by $\psi(z) = \psi(0)e^{-\varkappa z}$ with $\varkappa = \frac{\sqrt{2m(|U|-E)}}{\hbar}$ being the decay constant that describes an electron penetrating through the barrier into the $+z$ direction. The probability density for the observation of an electron near a point z is finite in the barrier region and is proportional to $|\psi(0)|^2 e^{-2\varkappa z}$. Additionally, electrons can propagate in the opposite direction ($-z$ -direction) indicating that tunneling is bidirectional. The total wave function in every region, sample, barrier and tip are written as:

$$\psi_S = e^{ikz} + Ae^{-ikz} \quad (2)$$

$$\psi_{\text{Barrier}} = Be^{-\varkappa z} + Ce^{\varkappa z} \quad (3)$$

$$\psi_T = De^{ikz} \quad (4)$$

The coefficients A , B , C and D take care of the reflection and transmission of the electrons, they are obtained by matching of the wave functions and their derivatives $d\psi/dz$ at the two interfaces, sample–barrier and barrier–tip. The incident current density $I_i = \hbar k/m$ and the transmitted current I_t

$$I_t = -i \frac{\hbar}{2m} \left(\psi_T^*(z) \frac{d\psi_T(z)}{dz} - \psi_T(z) \frac{d\psi_T^*(z)}{dz} \right) = \frac{\hbar k}{m} |D|^2 \quad (5)$$

Element	Al	Au	Cu	Ir	Ni	Pt	Si	W
Φ (eV)	4.1	5.4	4.6	5.6	5.2	5.7	4.8	4.8
\varkappa (\AA^{-1})	1.03	1.19	1.09	1.21	1.16	1.22	1.12	1.12

Table 1: Work functions and decay constants according to Ref. [22] for selected materials.

define the barrier transmission coefficient T which is given by the ratio between the transmitted current density and the incident current density:

$$T = \frac{I_t}{I_i} = |D|^2 = \frac{1}{1 + \frac{(k^2 + \varkappa^2)^2}{4k^2\varkappa^2} \cdot \sinh^2(\varkappa s)} \quad (6)$$

which simplifies in the limit of a strongly attenuating barrier (large decay constant \varkappa)

$$T \sim \frac{16\varkappa^2 k^2}{(k^2 + \varkappa^2)^2} \cdot e^{-2\varkappa s} \quad (7)$$

where s defines the location of electrode T (Fig. 2(b)).

From this basic model, some important features of a more realistic metal-vacuum-metal tunneling can be explained. Let us first evaluate the decay constant magnitude which is defined by the work function Φ primarily if the electrons involved in the tunneling process are lying close to the Fermi energy of both electrodes. Indeed Φ is defined by the minimum energy required to remove an electron from the bulk to the vacuum level. In general, the work function depends not only on the material, but also on the crystallographic orientation of the surface but to simplify our discussion we assume it to be the same for the tip and sample ($\Phi_S = \Phi_T = \Phi$). In our model $|U_S|$ and $|U_T|$ are respectively replaced by their respective work functions. Here the decay constant $\varkappa = \frac{\sqrt{2m\Phi}}{\hbar}$ is of the order of $\sim 1\text{\AA}^{-1}$ for the typical values of the work function ($\sim 5\text{eV}$). The typical values of work functions of materials used in STM experiments, together with the decay constants, are listed in Table 1. According to Eq. 7, the current decays by one order of magnitude per 1\AA .

Even though this model is too simple to describe realistic STM experiments it explains the high sensitivity to height changes in the sample topography. Also it demonstrates that during tunneling, the tip's atom, that is the closest to the substrate, is the main atom involved in the tunneling process!

From this simple one dimensional model one can derive the principle used by Binnig and Rohrer when they invented the STM. Their argument to explain the ability of STM to achieve large lateral resolutions and by that probe the electronic structures of various materials at an atomic scale ($\sim 2\text{\AA}$) is: because of the tunneling through vacuum, a large lateral resolution much smaller than the radius of the tip-end, R , is possible if the distance between the tip-end and the sample surface, Δz , is much smaller than the tip radius [46]. Near the tip-end, the current lines are almost perpendicular to the sample surface (Fig. 3). At a point Δx on the tip, the distance to the sample surface, z , is increased by

$$\Delta z \sim \frac{\Delta x^2}{2R}. \quad (8)$$

Assuming that at each point the tunneling current density follows the formula for the one-dimensional case, Eq. 7, the lateral current distribution is

$$I(\Delta x) \sim e^{-2\varkappa \frac{\Delta x^2}{2R}}. \quad (9)$$

Typically, $\kappa \sim 1\text{\AA}^{-1}$. For $R = 10\text{\AA}$, at $\Delta x \sim 4.5\text{\AA}$, the current drops by a factor of $\sim e^{-2}$, that is about one order of magnitude. The diameter of such a current column is the resolution limit, which is about 9\AA . Therefore with moderate means, a very high lateral resolution is expected. Nowadays, achievements of STM largely exceeds this expectation.

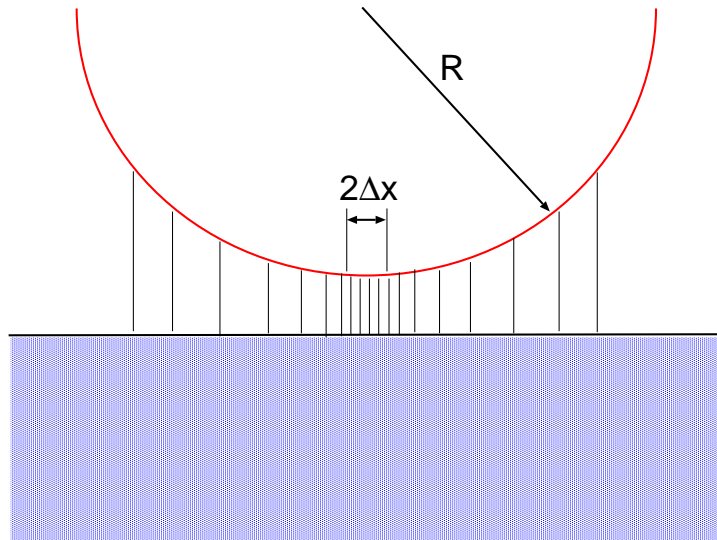


Fig. 3: Estimation of the lateral resolution in STM. Out of a spherical tip model with radius R very close to the surface, the lateral resolution of STM can be evaluated. The tunneling current is concentrated at the vicinity of the closest point to the substrate.

4 Modeling currents

4.1 Bardeen's approach

One-dimensional case

The planar tunneling junction problem treated by Bardeen is schematically shown in Fig. 2(b). The model used by Bardeen, called also the transfer Hamiltonian method [47], and extended later on by Tersoff and Hamann [23, 24] and Chen [25, 26] to STM, has naturally limitations by its assumptions but gives a fundamental understanding on the ability of STM to reach high space and energy resolution. Here are some assumptions that are assumed in the original derivation of the Bardeen's approach:

First of all, the electron tunneling is treated as a one-particle process, i.e. the mutual interaction between electrons during tunneling is neglected which is a reasonable approximation in the low tunneling regime. Furthermore, a direct interaction of tip and sample resulting in the formation of coupled electronic states is not taken into account. This assumption is valid if the tip-sample distance is large enough, i.e. a distance larger than $\sim 4\text{\AA}$ should be sufficient. Note that in our discussion elastic tunneling is assumed, i.e. no energy loss of the electrons with quasi-particles of the electrodes, e.g. plasmons, phonons, spin-excitations is considered in this section. Of course, recently models taking care of this kind of interactions were developed (see Chapter C 7 by M. Wegewijs for detailed examples) and a simple discussion on the treatment of inelastic tunneling is given later on in this manuscript.

When the two electrodes, representing the tip and the sample, are far apart, the wave functions of electrode S , representing the unperturbed substrate, or of the unperturbed electrode T , representing the tip, satisfy the Schrödinger equation of the free electrode S or T ,

$$i\hbar \frac{\partial \psi^i}{\partial t} = \left(-\frac{\hbar^2}{2m} \frac{\partial^2}{\partial z^2} + U_i \right) \psi^i, \quad (10)$$

where U_i is the potential function of electrode i (S or T), and ψ^i depends on both time and spatial coordinates. The stationary states are $\psi^i = \psi_\mu^i e^{-iE_\mu^i t/\hbar}$ with the spatial wave functions and energy eigenvalues satisfying

$$\left(-\frac{\hbar^2}{2m} \frac{\partial^2}{\partial z^2} + U_i \right) \psi_\mu^i = E_\mu^i \psi_\mu^i, \quad (11)$$

Once the distance between the two electrodes is reduced, the time-evolution of a state ψ in the system tip-sample is governed by the Schrödinger equation containing the full potential:

$$i\hbar \frac{\partial \psi}{\partial t} = \left(-\frac{\hbar^2}{2m} \frac{\partial^2}{\partial z^2} + U_S + U_T \right) \psi. \quad (12)$$

The time-evolution can be treated in perturbation theory. At $t \rightarrow -\infty$, the tip is far from the substrate and an electron is stationary in a state ψ_μ^S of the sample. We assume that the tip is approached slowly towards the sample and thereby the tip potential is turned on adiabatically. The adiabatic consideration is reasonable since the time-scale of electrons are femtoseconds ($\sim 10^{-15}$ sec) while the time needed to move the tip is in seconds. Formally we describe this adiabatic switching of the perturbation via a time-dependent potential

$$U_T(t) = e^{\eta t/\hbar} U_T, \text{ and } \eta > 0. \quad (13)$$

U_T is a constant and η is small and positive. At the end of our derivation, when we consider $\eta \rightarrow 0$, the potential will be constant for all times. With the presence of the combined potential, a state ψ_μ^S described by Eq. 11 at $t = -\infty$ will not evolve according to Eq. 10. Instead it has a probability of populating the states of electrode T , denoted as ψ_ν^T . Our goal is to measure that probability since it is directly related to the tunneling current.

The state ψ of the whole system can be expanded in a linear combination of the sample and tip eigenfunctions (as calculated before the perturbation is switched on), which form an orthogonal and complete basis set:

$$\psi = a_\mu(t) \psi_\mu^S e^{-iE_\mu^S t/\hbar} + \sum_{\nu=1}^{\infty} c_\nu(t) \psi_\nu^T e^{-iE_\nu^T t/\hbar}. \quad (14)$$

In our ansatz, $a_\mu(t)$ and $c_\nu(t)$ are coefficients to be determined by Eq. 12 with $a_\mu(-\infty) = 1$ and $c_\nu(-\infty) = 0$. We note that in our ansatz the time evolution coefficients $a_\mu(t)$ and $c_\nu(t)$ is due solely to the presence of the time dependence in $U_T(t)$. As we shall see, this separation is convenient because the time evolution coefficients satisfy a relatively simple differential equation.

It is important to note that each set of wave functions ψ_μ^S and ψ_ν^T originates from different Hamiltonians. Neither of them is an eigenfunction of the Hamiltonian of the combined system. A basic assumption of Bardeen's tunneling theory is that the two sets of wave functions are

approximately orthogonal, $\int \psi_\mu^{T*} \psi_\nu^S d^3r \approx 0$. Inserting Eq. 14 into Eq. 12 and after projection on the state ψ_ν^T , we obtain

$$i\hbar \frac{dc_\nu(t)}{dt} = \langle \psi_\nu^T | U_T | \psi_\mu^S \rangle e^{-i(E_\mu^S - E_\nu^T + i\eta)t/\hbar} + \sum_{\lambda=1}^{\infty} c_\lambda(t) \langle \psi_\nu^T | U_S | \Psi_\lambda^T \rangle e^{-i(E_\lambda^T - E_\nu^T)t/\hbar}. \quad (15)$$

Here we considered the following small approximations: (i) because of the adiabatic approximation we considered the prefactor $a(t)$ to be slowly varying, i.e. $\frac{d}{dt}a_\mu(t) = 0$ and $a_\mu(t) = 1$, and (ii) a second contribution $\sim (e^{\eta t/\hbar} - 1)$ is neglected since it vanishes at $\eta \rightarrow 0$.

This equation can be solved iteratively but we limit ourselves to the first order of time-dependent perturbation theory and neglect the second term on the right-hand side of the previous equation since it is a second-order infinitesimal quantity. Therefore, to first-order,

$$i\hbar \frac{dc_\nu(t)}{dt} = \langle \psi_\nu^T | U_T | \psi_\mu^S \rangle e^{-i(E_\mu^S - E_\nu^T + i\eta)t/\hbar}. \quad (16)$$

Since U_T is non-zero only in the volume of electrode T (at $z > s$, see Fig. 2), the integral $\langle \psi_\nu^T | U_T | \psi_\mu^S \rangle$, that defines the tunneling matrix element $M_{\mu\nu}$, is evaluated only in the right-hand side of the separation surface. This tunneling matrix element describes the projection of the initial state ψ_μ^S perturbed by the potential U_T onto the final state ψ_ν^T . After integration over time we get

$$c_\nu(t) = \frac{1}{E_\mu - E_\nu + i\eta} M_{\mu\nu} e^{-i(E_\mu^S - E_\nu^T + i\eta)t/\hbar}. \quad (17)$$

$|c_\nu(t)|^2$ describes the probability that an electron initially described by the state ψ_μ^S in time $t = -\infty$ populates a state ψ_ν^T at time t ,

$$|c_\nu(t)|^2 = \frac{e^{2\eta t/\hbar}}{(E_\mu^S - E_\nu^T)^2 + \eta^2} |M_{\mu\nu}|^2, \quad (18)$$

which leads to the tunneling probability per unit time, $P_{\mu\nu}(t) = \frac{d}{dt}|c_\nu(t)|^2$,

$$P_{\mu\nu}(t) = \frac{2\eta}{(E_\mu^S - E_\nu^T)^2 + \eta^2} e^{2\eta t/\hbar} \frac{1}{\hbar} |M_{\mu\nu}|^2, \quad (19)$$

where we can recognize the definition of the $\delta(x)$ distribution given by $\delta(x) = \frac{1}{\pi} \lim_{\eta \rightarrow 0} \frac{\eta}{x^2 + \eta^2}$.

Taking the limit $\eta \rightarrow 0$ we find

$$P_{\mu\nu}(t) = \frac{2\pi}{\hbar} \delta(E_\mu^S - E_\nu^T) |M_{\mu\nu}|^2, \quad (20)$$

which is the famous Fermi's Golden Rule, that is a general result of first order time-dependent perturbation theory (The Golden Rule is also derived in Chapter **A 5** by Ph. Mavropoulos). Elastic tunneling is guaranteed by the delta function $\delta(E_\mu^S - E_\nu^T)$. The tunneling current I is proportional to $eP_{\mu\nu}$ where e is the elementary electron charge.

Up to now we have considered the tunneling process involving a single state μ to a single state ν . However the tip and substrate are characterized by a continuous spectrum of states, thus we have to consider the sum over states μ and ν for every spin channel. Naturally an electron can only tunnel from an occupied state ψ_μ^S to an unoccupied state ψ_ν^T and vice-versa. At zero temperature, there is a sharp Fermi edge separating occupied and unoccupied states while at

elevated temperatures the Fermi edge is smeared out; occupied states are then described by the Fermi-Dirac distribution $f(E - E_F) = (1 + \exp[(E - E_F)/k_B T])^{-1}$ while unoccupied states are described by $1 - f(E - E_F)$. Accounting for the occupation in this manner and assuming a bias voltage V , the tunneling current in thermal equilibrium from sample to tip, $I_{S \rightarrow T}$, and from tip to sample, $I_{T \rightarrow S}$ can be written as:

$$I_{S \rightarrow T} = \frac{4\pi e}{\hbar} \sum_{\nu\mu} f(E_\mu^S - E_F^S) [1 - f(E_\nu^T - E_F^T)] |M_{\mu\nu}|^2 \delta(E_\nu^T - E_\mu^S - eV) \quad (21)$$

$$I_{T \rightarrow S} = \frac{4\pi e}{\hbar} \sum_{\nu\mu} f(E_\mu^T - E_F^T) [1 - f(E_\nu^S - E_F^S)] |M_{\mu\nu}|^2 \delta(E_\nu^T - E_\mu^S - eV)$$

A factor 2 has been introduced accounting for the two possible spin states of each electron. The difference between the two currents gives a net total tunneling current:

$$I = \frac{4\pi e}{\hbar} \sum_{\nu\mu} [f(E_\mu^S - E_F^S) - f(E_\nu^T - E_F^T)] |M_{\mu\nu}|^2 \delta(E_\nu^T - E_\mu^S - eV). \quad (22)$$

The finite summation over the discrete states can be replaced by an integral over energies using the density of state $n(E)$: $\sum_\mu \rightarrow \int n(E)dE$ and after an appropriate change of variable we find

$$I = \frac{4\pi e}{\hbar} \int d\epsilon [f(E_F^T - eV + \epsilon) - f(E_F^S + \epsilon)] \times n^T(E_F^T - eV + \epsilon) n^S(E_F^S + \epsilon) |M(E_F^S + \epsilon, E_F^T - eV + \epsilon)|^2 \quad (23)$$

where n^S and n^T are the density of states (DOS) of the substrate and of the tip. We find formally that the tunneling current depends explicitly on the electronic structure of both the tip and substrate which has important consequences on STM measurements. Interestingly at zero temperature or if $k_B T$ is smaller than the energy resolution required in the measurement, the Fermi distribution function can be approximated by a step function and the current simplifies to

$$I = \frac{4\pi e}{\hbar} \int_0^{eV} d\epsilon n^T(E_F^T - eV + \epsilon) n^S(E_F^S + \epsilon) |M|^2 \quad (24)$$

and for a very small bias voltage

$$I = \frac{4\pi e}{\hbar} V n^T(E_F^T) n^S(E_F^S) |M|^2. \quad (25)$$

The differential conductivity, which is the other quantity measured experimentally, is given by

$$\frac{dI}{dV} = \frac{4\pi e}{\hbar} n^T(E_F^T) n^S(E_F^S + eV) |M(E_F^S + eV, E_F^T)|^2. \quad (26)$$

This explains the unique power of STM to be able to access the occupied and unoccupied electronic states of the substrate. Indeed this can be achieved by changing the sign of the bias voltage V .

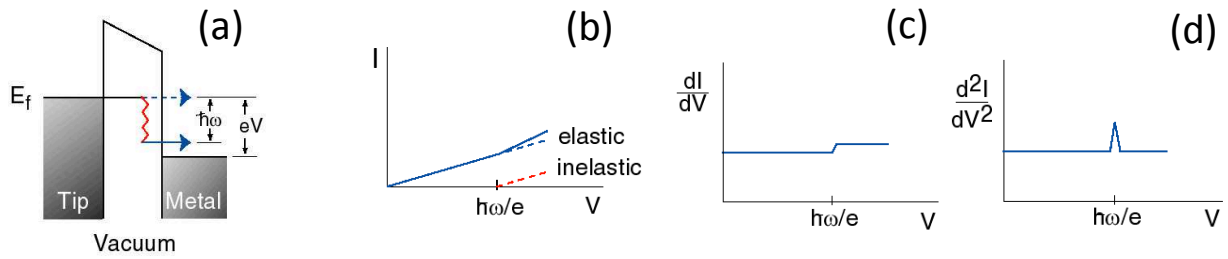


Fig. 4: Schematic representation of inelastic tunneling with STM (according to Wilson Ho) is shown in (a). If the electron has enough energy, provided by the bias potential, to trigger the excitation mode an additional tunneling channel is created. The slope giving the tunneling current versus the bias voltage (b) changes at a bias voltage corresponding to the frequency of the excitation mode. Taking the first and second derivatives lead to a step-like function (c) or to a resonance (d) at $\hbar\omega$.

Inelastic tunneling

Although the rest of this lecture is devoted to elastic tunneling phenomena, inelastic tunneling within the Bardeen approach is described briefly in this section. Within STM, these excitations were observed for vibrations (see e.g. [14]), photons (see e.g. [19]) and for spin-excitations (see e.g. [15, 16, 17, 18, 57]).

We have learned earlier that the current and differential conductivity is proportional to the DOS of the substrate and of the tip. Now imagine that on the substrate a molecule is deposited which is characterized by a vibrational mode or a spin excitation mode. If the tunneling current can trigger the excitation, i.e. the tunneling electrons couple to the excitation mode and by that loose their energy, additional tunneling channels can be created. More tunneling possibilities translates to an increase in the tunneling current. Fig. 4 shows schematically how the slope of the current versus the bias voltage increases suddenly at the voltage, or energy, corresponding to the excitation mode. If one calculates or measures the differential conductivity, one obtains step-like functions in the spectra, and a second derivative of the current leads to resonances located at the excitation energies.

Consider that the potential of the sample U_S contains a vibrating adatom and is time-dependent $U_S + U_0 \cos(\omega t)$, where U_0 is the amplitude of the vibration and ω is the vibrational frequency of the adatom. We apply once more first order time-dependent perturbation theory as discussed previously and find:

$$i\hbar \frac{dc_\nu(t)}{dt} = M_{\mu\nu} e^{-i(E_\mu^S - E_\nu^T + i\eta)t/\hbar} + \delta M_{\mu\nu} \cos(\omega t) e^{-i(E_\mu^S - E_\nu^T)t/\hbar} \quad (27)$$

where $M_{\mu\nu}$ is the elastic tunneling matrix element $\langle \psi_\nu^T | U_T | \psi_\mu^S \rangle$ and $\delta M_{\mu\nu}$ is the inelastic counterpart $\langle \psi_\nu^T | U_0 | \psi_\mu^S \rangle$.

After integration, the inelastic contribution to the coefficient c_ν in Eq. 27 is

$$\delta c_\nu(t) = \frac{\delta M_{\mu\nu}}{2} \left[\frac{e^{(E_\mu - E_\nu + \hbar\omega)t/\hbar}}{E_\mu - E_\nu + \hbar\omega} + \frac{e^{(E_\mu - E_\nu - \hbar\omega)t/\hbar}}{E_\mu - E_\nu - \hbar\omega} \right]. \quad (28)$$

The probability is thus simply given by²

$$|\delta c_\nu|^2 = |\delta M_{\mu\nu}|^2 \left(\frac{\sin^2[(E_\mu - E_\nu + \hbar\omega)t/2\hbar]}{(E_\mu - E_\nu + \hbar\omega)^2} + \frac{\sin^2[(E_\mu - E_\nu - \hbar\omega)t/2\hbar]}{(E_\mu - E_\nu - \hbar\omega)^2} + \text{cross terms} \right).$$

The function $\sin^2(xt/2\hbar)/x^2$ reaches its maximum when $x = 0$ and approach rapidly zero for $x \neq 0$. In the limit of long time t , this function is nothing else than a delta function: $t\pi\delta(x)/2\hbar$, which ensures that the inelastic tunneling occurs at $E_\mu - E_\nu - \hbar = \pm\hbar\omega$. Finally we give the probability rate as done in the previous section:

$$\delta P_{\mu\nu} = \frac{d|\delta c_\mu|^2}{dt} \propto \frac{\pi}{2\hbar} |\delta M_{\mu\nu}|^2 \delta(E_\mu - E_\nu \pm \hbar\omega) \quad (29)$$

Therefore in addition to the elastic tunneling term, we have an additional term when the excitation is created, i.e. the energy level of the electronic state changes by an amount $\hbar\omega$. We note that several theoretical methods were developed in order to understand how STM probes excitations. For instance, for spin-excitations, some are based on a Heisenberg Hamiltonian (see e.g. Refs.[29, 30, 31, 32]) and beyond[33], others are based on time-dependent density functional theory [34, 35].

Bardeen's Tunneling Matrix elements

We derived earlier the tunneling current and the differential conductivity in the Bardeen's approach, we investigate in the following the tunneling matrix element $M_{\mu\nu}$. Using Eq. 11, the integral defining the tunneling matrix element $M_{\mu\nu} = \langle \psi_\nu^T | U_T | \psi_\mu^S \rangle$ can be converted into a surface integral only depending on the unperturbed wave functions of the two electrodes at the separation surface. By applying Eq. 11, we have

$$M_{\mu\nu} = \int_{z>z_0} \psi_\mu^S \left(E_\nu^T + \frac{\hbar^2}{2m} \frac{\partial^2}{\partial z^2} \right) \psi_\nu^{T*} d^3r. \quad (30)$$

Because of the elastic tunneling condition, $E_\mu^S = E_\nu^T$, the form giving the tunneling matrix element can be converted into

$$M_{\mu\nu} = \int_{z>z_0} \left(\psi_\mu^S E_\mu^S \psi_\nu^{T*} + \psi_\mu^S \frac{\hbar^2}{2m} \frac{\partial^2}{\partial z^2} \psi_\nu^{T*} \right) d^3r. \quad (31)$$

Using $M_{\mu\nu} = \langle \psi_\mu^S | U_T | \psi_\nu^T \rangle$ and noticing that, on the tip side, the sample potential U_S is zero, we obtain

$$M_{\mu\nu} = -\frac{\hbar^2}{2m} \int_{z>z_0} \left(\psi_\nu^{T*} \frac{\partial^2 \psi_\mu^S}{\partial z^2} - \psi_\mu^{*S} \frac{\partial^2 \psi_\nu^T}{\partial z^2} \right) d^3r. \quad (32)$$

With the identity

$$\psi_\nu^{T*} \frac{\partial^2 \psi_\mu^S}{\partial z^2} - \psi_\mu^{*S} \frac{\partial^2 \psi_\nu^T}{\partial z^2} = \frac{\partial}{\partial z} \left[\psi_\nu^{T*} \frac{\partial \psi_\mu^S}{\partial z} - \psi_\mu^S \frac{\partial \psi_\nu^{T*}}{\partial z} \right], \quad (33)$$

the integration over z can be carried out to obtain

$$M_{\mu\nu} = \frac{\hbar^2}{2m} \int_{z=z_0} \left[\psi_\mu^S \frac{\partial \psi_\nu^{T*}}{\partial z} - \psi_\nu^{T*} \frac{\partial \psi_\mu^S}{\partial z} \right] dx dy. \quad (34)$$

²Other cross terms are not considered here

The last equation gives Bardeen's tunneling matrix element in a one-dimensional form. It is a surface integral of the wave functions (and its normal derivatives) of the two free electrodes, evaluated at the separation surface. The potential barrier information does not appear explicitly, and only the information of the wave functions at the separation surface is required. Furthermore, the formula is symmetric with regards to both electrodes. It is the basis of the reciprocity principle in STM, which has important consequences in designing and interpreting experimental results.

Although derived for the one-dimensional case, the Bardeen approach can be extended to the three-dimensional case where the tunneling matrix element, Eqs. 32 and 34, change to

$$M_{\mu\nu} = \frac{\hbar^2}{2m} \int_{\Omega_T} [\psi_\mu^S \Delta \psi_\nu^{T*} - \psi_\nu^{T*} \Delta \psi_\mu^S] \cdot d\vec{r} \quad (35)$$

and

$$M_{\mu\nu} = \frac{\hbar^2}{2m} \int_{\Sigma} [\psi_\mu^S \vec{\nabla} \psi_\nu^{T*} - \psi_\nu^{T*} \vec{\nabla} \psi_\mu^S] \cdot d\vec{S} \quad (36)$$

where the surface integral is performed on the separation surface, Σ , between the volume defining the sample and the volume defining the tip.

Energy dependence of tunneling matrix elements

The assumption, that the tunneling matrix element M is a constant, is reasonable for a small bias voltage window. However, in scanning tunneling spectroscopy (STS) experiments, the energy scale can be as large as $\pm 2eV$. Thus the energy dependence of the tunneling matrix element cannot be overlooked. The variation of $|M|$ with energy can be evaluated from the Bardeen formula, Eq. 34.

In the gap region, the wave function of electrode S is:

$$\psi_\mu^S(z) = \psi_\mu^S(0) e^{-\kappa_\mu^S z}, \quad (37)$$

where $\kappa_\mu^S = \sqrt{2m|E_\mu^S|}/\hbar$ is the decay constant corresponding to the energy eigenvalue of ψ_μ^S . Similarly, in the gap region, the wave function of electrode T is

$$\psi_\nu^T(z) = \psi_\nu^T(s) e^{\kappa_\nu^T(z-s)}. \quad (38)$$

Because of the condition of elastic tunneling ($E_\mu^S = E_\nu^T$), the two decay constants are equal,

$$\kappa_\nu^T = \kappa_\mu^S = \frac{\sqrt{2mE_\mu^S}}{\hbar} \quad (39)$$

Inserting the previous equations into Eq. 34, we obtain

$$M_{\mu\nu} = \frac{\hbar^2}{2m} e^{-\kappa_\mu^S s} \int_{z=z_0} 2\kappa_\mu^S \psi_\mu^S(0) \psi_\nu^T(s) dx dy. \quad (40)$$

As expected, the tunneling matrix element is independent of the position of the separation surface, $z = z_0$. The expression in the integral is a constant, because $\psi_\nu^T(s)$ is the value of the wave function of electrode T at its surface. The energy dependence of M is through the decay

constant κ_{μ}^S . Qualitatively, the effect of the energy dependence of the tunneling matrix element on the tunneling current is as follows. Once the integration over energies is carried out in Eq. 24, we realize that the value of $e^{-\kappa_{\mu}^S s}$ near the top of the integral is bigger than its value near the bottom. Therefore, the energy spectrum of electrode T near the Fermi level and the empty states energy from the spectrum of electrode S electrons about eV above the Fermi level are the dominant contributors to the integral in Eq. 24.

We have learned from the Bardeen's approach to calculate the tunneling current, that the exact electronic structure of tip and sample is required. In principle it is possible to calculate them for both systems with the actually available ab-initio methods and to compute all tunneling matrix elements to gain the tunneling current. Although quite elaborate, this scheme is possible. However, the tip structure is not straightforward to access experimentally which complicates the task of simulating the STM tip. This issue pushed the development of models, as the one described in the next section, that simplify the tip's electronic structure. The simplest approach is to get rid off the tip.

4.2 Tersoff-Hamann model

After the invention of STM, Tersoff and Hamann formulated a model [23, 24] based on Bardeen's tunneling theory which is widely used today. Here we describe its concept, derivation and limitations.

The essence of the model

The driving argument behind the Tersoff-Hamann (TH) model is the difficult access to the tip states. Those, as we have learned in the previous sections, are important in the imaging mechanism of STM since the tunneling current is a convolution of electronic states of the tip to those of the sample. Therefore, a particular model of the tip was proposed, such that the tip properties can be simplified and factorized out of the problem. The TH model represents the tip with potential and wave functions arbitrarily localized, in words, modeled as a geometrical point. Consequently, the STM image is related to the properties of the surface alone. Thus, according to that model, STM measures an intrinsic property of the unperturbed surface, rather than a property of the joint surface-tip system.

The TH model has proven to be extremely valuable in interpreting the STM images with characteristic feature sizes of $\geq 10\text{\AA}$, for example, the profiles of superstructures of surface reconstruction, the scattered waves of surface states, as well as defects, adsorbates, and substitution atoms on the surface. However, the TH model predicts that the corrugation of atomic-scale features (with typical length scale close to or smaller than 3\AA) is about one picometer or even smaller, which is beyond the detection limit of STM. Also it cannot always explain the rich experimental observations due, obviously, to the convolution of tip electronic states and sample electronic states.

Derivation of TH model

The STM tip is modeled as a locally spherical potential well centered at \vec{R}_T . Once more, the sample surface is represented by the $z = 0$ plane. In Bardeen's model the potentials of the tip and sample are negligible in the separation plane Σ . Therefore in the vacuum region, both wave

functions of sample and tip near the Fermi level satisfy the Schrödinger equation

$$-\frac{\hbar^2}{2m}\Delta\psi = -\Phi\psi \quad \text{or} \quad \Delta\psi = \varkappa^2\psi, \quad (41)$$

With the approximation that the tip is just a single atom which has an s -orbital as wave function, this equation has two solutions, an irregular and a regular solution, which are the spherical, modified Bessel functions of first and second kind. We are interested in the regular solution that is characterized by an exponential decay from tip to vacuum. Thus the solution of the previous equation is given by the modified Bessel function of the second kind

$$\psi_\nu^T(\vec{r} - \vec{R}_T) = Ck_0^{(1)}(\varkappa|\vec{r} - \vec{R}_T|) = C\frac{e^{-\varkappa|\vec{r} - \vec{R}_T|}}{\varkappa|\vec{r} - \vec{R}_T|} \quad (42)$$

where $|\vec{r} - \vec{R}_T| \neq 0$ since the solution is obtained in the vacuum at position \vec{r} and C is a normalization constant.

Inserting this ansatz for the tip wave function into the expression for the matrix tunneling element (Eq. 35) yields

$$M_{\mu\nu}(\vec{R}_T) = -\frac{C\hbar^2}{2m} \int_{\Omega_T} \left[k_0^{(1)}(\varkappa|\vec{r} - \vec{R}_T|)\Delta\psi_\mu^S(\vec{r} - \vec{R}_T) - \psi_\mu^S(\vec{r} - \vec{R}_T)\Delta k_0^{(1)}(\varkappa|\vec{r} - \vec{R}_T|) \right] d\vec{r}. \quad (43)$$

Since the sample potential vanishes in the body of the tip we can apply the vacuum Schrödinger equation to the first term of the integrand. The second term has a singularity at $\vec{r} = \vec{R}_T$ and can be simplified recalling the relation between the modified Bessel function $k_0^{(1)}$ and the Green function of the vacuum Schrödinger equation:

$$\Delta G(\vec{r} - \vec{r}') = -4\pi\delta(\vec{r} - \vec{r}'). \quad (44)$$

Since $G(\vec{r} - \vec{r}') = \varkappa k_0^{(1)}(\varkappa|\vec{r} - \vec{r}'|)$, we rewrite $\Delta k_0^{(1)}$ in Eq. 43 as $(\varkappa^2 k_0^{(1)} - 4\pi\delta/\varkappa)$ and by that the tunneling matrix element for the case of a s -wave function simplifies in the TH model to

$$M_{\mu\nu}(\vec{R}_T) = -\frac{2\pi C\hbar^2}{\varkappa m} \psi_\mu^S(\vec{R}_T) \quad (45)$$

This is the central result of the TH model of STM although the original derivation is a bit longer. If the tip state is spherically symmetric around a point \vec{R}_T , effectively, it is equivalent to a geometrical point at \vec{R}_T . Hence, the tunneling matrix element is directly proportional to the value of the sample wave function at the position of the apex atom. Now we are able to calculate the tunneling current following Bardeen's formulation at low temperature:

$$I(\vec{R}_T, V) = \frac{16\pi^3 C^2 \hbar^3 e}{\varkappa^2 m^2} n^T \int_0^{eV} d\epsilon n^S(\vec{R}_T, E_F^S + \epsilon) \quad (46)$$

where n^T is a constant in the TH model since the wave function of the tip is of s -type and $n^S(\vec{R}_T, \epsilon) = \sum_\mu \delta(E_\mu^S - \epsilon) |\psi_\mu^S(\vec{R}_T)|^2$. Eq. 46 expresses that the integral includes all states of the sample at the tip location between the Fermi energy and the Fermi energy shifted by the applied bias voltage: the tunneling current is proportional to the integrated local density of states (ILDOS) of the sample.

For a small bias voltage, the previous equation simplifies further to

$$I(\vec{R}_T, V) = \frac{16\pi^3 C^2 \hbar^3 e^2}{\kappa^2 m^2} V n^T n^S(\vec{R}_T, E_F^S). \quad (47)$$

For the differential conductivity we obtain for finite V

$$\frac{dI(\vec{R}_T, V)}{dV} = \frac{16\pi^3 C^2 \hbar^3 e}{\kappa^2 m^2} n^T n^S(\vec{R}_T, E_F^S + eV). \quad (48)$$

Thus the tunneling current and the differential conductivity are proportional to the density of states $n^S(\vec{R}_T, E_F^S + eV)$ in the vacuum. The last three equations are the most used ones in the interpretation, simulation and prediction of STM-images for realistic systems. We note that an absolute value of the current within this scheme cannot be computed since the constant C is unknown. From the TH model, one can simulate the important STM modes mentioned in Section 2. For example, in the constant-current mode ($I = \text{const.}$), where topographic images are obtained, we use $I \sim eV n^S(\vec{R}_T, E_F^S)$ valid for $eV \ll \Phi$. Hence, the task is simply to look for $n^S(\vec{R}_T, E_F^S) = \text{const.}$ In the spectroscopic mode, dI/dV is computed from $\sim n^S(\vec{R}_T, E_F^S + eV)$, in other words the calculation of the spectroscopic images obtained with STM boils down to the computation of the sample's DOS in vacuum.

The basic assumption of this extremely simple result is that, except for the s -wave tip wave function, all other tip wave functions can be neglected. Therefore it is often called the s -wave tip model. It is important to know under which condition the s -wave-only assumption is valid. The TH model is highly valuable in the interpretation of STM images. It represents an approximation with which the complicated problem of tip electronic states can be avoided.

What if the STM-tip is more complicated than what is assumed in the TH-model? For example, other orbitals, than the s , can be characterizing the apex atom. Chen [25, 26] proposed an elegant method, discussed in the upcoming subsection, that extends the TH-model.

Chen's expansion of the Tersoff-Hamann model

The problems which arise from the Tersoff-Hamann model can be overcome by expanding the model using generalized wave functions for the tip. Such an expansion was introduced by Chen [25, 26] who considered the general solutions of the vacuum Schrödinger equation (Eq. 41)

$$\psi^T(\vec{r} - \vec{R}_T) = \sum_{l,m} C_{lm} k_l^{(1)}(\kappa|\vec{r} - \vec{R}_T|) Y_{lm}(\widehat{|\vec{r} - \vec{R}_T|}) \quad (49)$$

where Y_{lm} are the spherical harmonics and $k_l^{(1)}$ are modified spherical Bessel functions of the second kind while C_{lm} is a renormalization coefficient. For the case $l = 0$ we recover the TH model as detailed in the previous subsection. Using the property of the Bessel function:

$$k_l^{(1)}(u) = (-1)^l u^l \left(\frac{1}{u} \frac{d}{du} \right)^l k_0^{(1)}(u) \quad (50)$$

one can evaluate the contribution of a tip-orbital l to the tunneling current just by proceeding to the l^{th} derivative with respect to the argument of modified Bessel function with $l = 0$. For

example, if the tip is described by a p_z -type orbital we have

$$\begin{aligned}\psi_{p_z}^T(\vec{r} - \vec{R}_T) &= C_{p_z} k_1^{(1)}(\kappa|\vec{r} - \vec{R}_T|) Y_{10}(\widehat{|\vec{r} - \vec{R}_T|}) \\ &= C_{p_z} \frac{d}{dR} k_0^{(1)}(\kappa|\vec{r} - \vec{R}_T|) \frac{\partial R}{\partial z} \\ &= \frac{C_{p_z}}{C_s} \frac{\partial}{\partial z} \psi_s^T(\vec{r} - \vec{R}_T).\end{aligned}\quad (51)$$

Inserting this wave function in the Bardeen's formula for the tunneling matrix elements in the TH model, we obtain for the p_z orbital

$$M_{\mu\nu} = -\frac{2\pi C_{p_z} \hbar^2}{\kappa m} \frac{\partial}{\partial z} \psi_\mu^S(\vec{R}_T). \quad (52)$$

This means, that the matrix element is proportional to the derivative of the sample wave function with respect to Z at the position of the tip, if the tip is described by a p_z -type orbital. In this way the matrix element can be derived also for higher order orbitals, which is known as the derivative rule of Chen [25, 26].

Using p - or d -type orbitals for the tip, the experimentally observed corrugation amplitudes of densely packed metal surfaces can be explained. In Table 4.2 the tunneling matrix elements are given for different orbitals. With the help of this rule, Chen could explain the high corrugation amplitude observed in some systems.

The extension of Chen provides an explanation of the high corrugation amplitudes measured on close-packed metal surfaces contradictory to the low corrugation amplitudes due to their local density of states. This is the case, for example, for p_z and d_{z^2} orbitals since they possess charge density stretching out further from the tip apex into the vacuum than that of an s -wave and they act similar to an s -wave at a reduced distance from the sample surface. This affects the tunneling current quite strongly and by that the images obtained experimentally. Interestingly, orbitals like d_{xy} and $d_{xz,yz}$ are expected to produce a large tunneling current not with the tip apex atom located on top of a surface atom but rather at a hollow site of the surface. Due to their particular charge density distribution a large overlap with sample orbitals occurs in this configuration.

4.3 Different STM modes

Now that we know how to compute the tunneling current, it is interesting to connect this quantity to the different STM standard modes. For a given bias, the physical quantity measured by the STM is the tunneling current, which is a function of the lateral coordinates (x, y) and the z -coordinate: $I = I(x, y, z)$. If z is perpendicular to a nearly flat surface, the tunneling current can be decomposed into a constant (that is independent of (x, y)) and a small variable component that represents the features or corrugation of the surface,

$$I(x, y, z) = I_0(z) + \Delta I(x, y, z), \quad (53)$$

with the condition $|\Delta I(x, y, z)| \ll |I_0(z)|$.

The constant-current topographic image can be derived from the current images by making the ansatz: $z(x, y) = z_0 + \Delta z(x, y)$ and substituting it into the previous equation by proceeding to a Taylor expansion we find

$$I = I_0(z_0) + \left(\frac{dI_0(z)}{dz} \right) \Delta z(x, y) + \Delta I(z, y, z). \quad (54)$$

Orbital of the tip	Matrix element M
s	$\frac{2\pi Ch^2}{\varkappa m} \psi^S(\vec{R}_T)$
p_x	$\frac{2\pi Ch^2}{\varkappa m} \frac{\partial}{\partial x} \psi^S(\vec{R}_T)$
p_y	$\frac{2\pi Ch^2}{\varkappa m} \frac{\partial}{\partial y} \psi^S(\vec{R}_T)$
p_z	$\frac{2\pi Ch^2}{\varkappa m} \frac{\partial}{\partial z} \psi^S(\vec{R}_T)$
d_{zx}	$\frac{2\pi Ch^2}{\varkappa m} \frac{\partial^2}{\partial z \partial x} \psi^S(\vec{R}_T)$
d_{zy}	$\frac{2\pi Ch^2}{\varkappa m} \frac{\partial^2}{\partial z \partial y} \psi^S(\vec{R}_T)$
d_{xy}	$\frac{2\pi Ch^2}{\varkappa m} \frac{\partial^2}{\partial x \partial y} \psi^S(\vec{R}_T)$
$d_{z^2 - \frac{1}{3}r^2}$	$\frac{2\pi Ch^2}{\varkappa m} \left(\frac{\partial^2}{\partial z^2} \psi^S(\vec{R}_T) - \frac{1}{3} \varkappa^2 \psi^S(\vec{R}_T) \right)$
$d_{x^2 - y^2}$	$\frac{2\pi Ch^2}{\varkappa m} \left(\frac{\partial^2}{\partial x^2} \psi^S(\vec{R}_T) - \frac{\partial^2}{\partial y^2} \psi^S(\vec{R}_T) \right)$

Table 2: Tunneling matrix elements as formulated by Chen [22] using the derivative rule. Note that the constant C depends on the orbital-type of the tip involved in the tunneling process.

Owing to the smallness of ΔI , its variation can be neglected. The topographic image is therefore defined by the condition of constant current, i.e. $I = I_0(z_0)$, thus

$$\Delta z(x, y) = -\frac{\Delta I(x, y)}{dI_0(z)/dz}. \quad (55)$$

It is interesting to note that experimentally when scanning the sample surface with the tip there are two different modes of operation, the constant-height and the constant-current mode. In constant-height mode, the vertical position z of the tip is held constant while scanning and the resulting tunnel current between tip and sample is measured. In constant-current mode a feedback loop provides a constant tunnel current between tip and sample at every position (x, y) . This means that the z -position of the tip has to be adjusted during scanning which is done by applying an appropriate voltage V_z to the z -piezo of the tube scanner. One distinguishes between these two extreme modes of operation even though neither of them can be realized experimentally and one can only approximate one or the other by choosing the appropriate parameters for the feedback loop gain and the scan speed.

The differential tunneling conductivity, dI/dV , is also a frequently used image parameter. Experimentally the tunneling spectrum at each point (x, y) can be obtained by interrupting the feedback circuit, applying a voltage ramp, then acquiring the tunneling current. The differential tunneling conductivity can be obtained by numerically differentiating the acquired tunneling current data.

4.4 Spin-polarization and tunneling: SP-STM and TAMR-STM

If the tunnel current flows between two magnetic electrodes, an additional information will be contained in the tunneling current, namely the information on the magnetic properties of the electrodes. Thus, if the STM tip is spin-polarized, in other words, the DOS for the majority-spin (\uparrow) channel is different from the DOS for the minority-spin (\downarrow) channel, access to the local spin-polarization of the probed substrate is possible (Figs. 5(a) and (b)). This is the concept of spin-polarized STM (SP-STM). By assuming that the electron spin is conserved during the tunneling process, the \uparrow -electrons from the tip can only tunnel into unoccupied \uparrow -states in the sample; the same for the \downarrow -electrons (Fig. 5(b)). When the magnetization directions of the two electrodes are in parallel alignment the tunnel current is different compared to the antiparallel alignment.

In fact Jullière [48] first discovered this spin valve effect, or tunneling magnetic resistance (TMR), in planar Fe-Ge-Co tunnel junctions effect which showed a decreased conductance in the case of non-parallel alignment of the electrodes magnetization compared to the parallel case. In a theoretical work, Slonczewski extended the model of tunneling in one dimension considering spin-polarized electrodes [49]. While the experiments of Jullière had to be realized at very low temperatures, the TMR effect at room temperature was achieved in the 90's by Moodera [50] and Miyazaki [51]. This allows for the application of the TMR effect in read heads of modern hard disk drives. Furthermore, the discovery of the TMR gave rise to the development of the magneto-resistive random-access memory (MRAM) – a non-volatile random-access memory technology.

Due to spin-orbit coupling (SOC), the resistance can become anisotropic, i.e., it depends on the magnetization direction of the tunnel junction with respect to the crystallographic axes as sketched in Fig. 5(c). For the observation of this effect the tunneling junction needs only a single magnetic electrode separated from a nonmagnetic electrode by an insulating layer. In

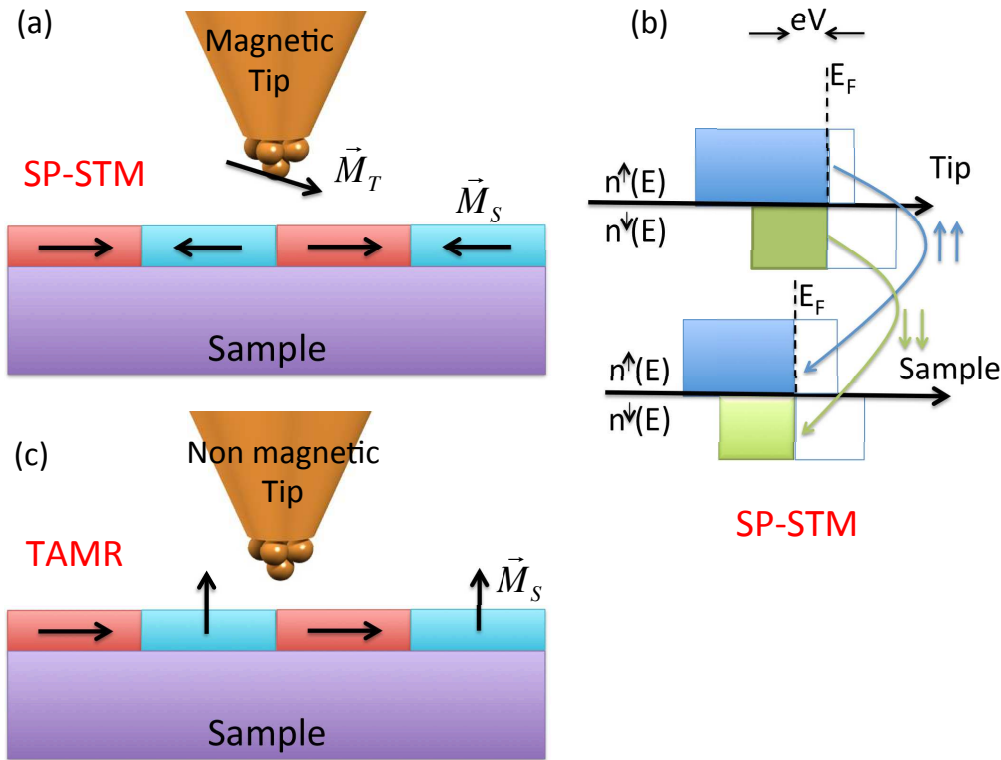


Fig. 5: Spin-polarized tunneling with SP-STM shown schematically in (a) and (b). In (b), the spin-polarized DOS of the tip and sample are depicted. With spin conservation, electrons from the tip with spin \uparrow can tunnel into unoccupied states of the sample with the same spin character. The same tunneling process occurs with spin \downarrow . In (c) a sketch of TAMR is shown. The tunnel junction comprises a non-magnetic tip and a magnetic sample. Because of spin-orbit coupling the tunneling current can be sensitive to the magnetization's orientation of the sample.

fact depending on the magnetization direction, the electronic structure of the magnetic electrode changes, thus the tunneling current between the two electrodes exhibits differences for a film that is magnetized either out-of-plane or in-plane [52, 53]. This effect has been named tunneling anisotropic magneto-resistance (TAMR) [53] which is an extension of the known bulk AMR that does not involve tunneling. Besides its implications in spintronics, it is appealing to use the TAMR concept in STM since even without a spin-polarized tip, magnetic information can be grasped from the tunneling current if the sample is characterized by a non-negligible SOC. The TAMR has first been observed in STM measurements of a double-layer film of Fe on the W(110) surface [52] and was recently applied on adatoms deposited on magnetic substrates [54, 55]. Since more than 10 years, SP-STM is a well-established technique which can be used to investigate the magnetic ground state of nanostructures down to the atomic scale [9]. In the past years, the technique has been extended to study also dynamics of magnetic systems like spin-flip processes [15, 16, 17, 18] or magnon excitation [57]. Furthermore, very recently SP-STM has been used to probe spin relaxations of single atoms on the time scale of nanoseconds [58, 59] to few minutes [60].

In the following two subsections, the basic theoretical concepts behind SP-STM and TAMR

within STM are presented.

Bardeen's formalism for SP-STM

The Bardeen tunneling theory can be extended to include the spin dependence. Instead of using a single-component wave function, two components, i.e. a spinor, are necessary to describe a state of an electron with spin. For example, for the sample wave function

$$\psi_{\mu\sigma}^S = \sum_{\sigma'=\uparrow,\downarrow} \psi_{\mu\sigma\sigma'}^s \chi_{\sigma'}, \quad \text{with } \chi_{\uparrow} = \begin{pmatrix} 1 \\ 0 \end{pmatrix}, \chi_{\downarrow} = \begin{pmatrix} 0 \\ 1 \end{pmatrix}. \quad (56)$$

One can follow the same procedure as done previously in Section 4.1 for the non spin-polarized case by considering the time-dependent Pauli equation of the combined system

$$i\hbar \frac{\partial \psi}{\partial t} = \left[-\frac{\hbar^2}{2m} \nabla^2 + \hat{U}_T + \hat{U}_S \right] \psi. \quad (57)$$

Note that the wave function ψ is now a two-component spinor and the potential functions are now two-by-two matrices,

$$\hat{U}_T = \begin{pmatrix} U_{T\uparrow\uparrow} & U_{T\uparrow\downarrow} \\ U_{T\downarrow\uparrow} & U_{T\downarrow\downarrow} \end{pmatrix}, \hat{U}_S = \begin{pmatrix} U_{S\uparrow\uparrow} & U_{S\uparrow\downarrow} \\ U_{S\downarrow\uparrow} & U_{S\downarrow\downarrow} \end{pmatrix}, \quad (58)$$

We follow the treatment of Wortmann *et al.* [61] to take the spin-polarization direction of one of the electrodes, say, electrode T, as the reference (global spin frame of reference). In other words, we assume that the Hamiltonian of the tip is diagonal with respect to spin,

$$\hat{U}_T = \begin{pmatrix} U_{T\uparrow\uparrow} & 0 \\ 0 & U_{T\downarrow\downarrow} \end{pmatrix}. \quad (59)$$

Therefore, the two components of the wave functions of the tip-only system can be treated separately to satisfy the following equation (considering the tip only),

$$\left[-\frac{\hbar^2}{2m} \nabla^2 + U_{T\sigma\sigma} \right] \psi_{\nu\sigma\sigma}^T(\vec{r}) = E_{\nu\sigma\sigma} \psi_{\nu\sigma\sigma}^T(\vec{r}), \quad (60)$$

where σ denotes the spin component \uparrow or \downarrow .

However, in the reference frame of the tip, the state of electrode S is, in general, not diagonalized with respect to spin. This is evidently true for non-collinear systems since no quantization axis exists which allows a state to be written in terms of pure spin-up or spin-down character, but even for collinear samples the states will be spin mixed if the quantization axis of the sample and the one of the tip are not aligned in parallel. In general, the spinor of the sample-only system satisfies the Pauli equation,

$$\left[-\frac{\hbar^2}{2m} \nabla^2 + \begin{pmatrix} U_{S\uparrow\uparrow} & U_{S\uparrow\downarrow} \\ U_{S\downarrow\uparrow} & U_{S\downarrow\downarrow} \end{pmatrix} \right] \begin{pmatrix} \psi_{\mu\uparrow\sigma}^S \\ \psi_{\mu\downarrow\sigma}^S \end{pmatrix} = \hat{E}_\mu \begin{pmatrix} \psi_{\mu\uparrow\sigma}^S \\ \psi_{\mu\downarrow\sigma}^S \end{pmatrix}. \quad (61)$$

It is useful to express the components of spinor describing the sample's wave function in the spin-frame of reference of the tip within the local spin frame of reference related to the sample.

In this local spin-frame of reference \hat{U}_S is diagonal in spin-space. This can be achieved using the rotation matrix \hat{U} .

$$|\psi_\sigma^S\rangle = \hat{U}(\theta)|\psi_\sigma^{S,loc}\rangle, \quad \text{with } \hat{U}(\theta) = \begin{pmatrix} \cos(\theta/2) & -\sin(\theta/2) \\ \sin(\theta/2) & \cos(\theta/2) \end{pmatrix}, \quad (62)$$

where *loc* stands for local spin-frame of reference of the sample and θ defines the angle between the magnetization of the individual atom on the sample and the magnetization of the tip.

Following the same procedure as done in the non spin-polarized case, we find in first-order perturbation theory that the spin-dependent tunneling matrix elements are given by

$$M_{\mu\nu}^{\sigma\sigma'} = \langle \psi_{\mu\sigma'}^T | \hat{U}_T \hat{U}(\theta) | \psi_{\mu\sigma}^{S,loc} \rangle \quad (63)$$

and

$$\begin{pmatrix} M_{\mu\nu}^{\uparrow\uparrow} & M_{\mu\nu}^{\uparrow\downarrow} \\ M_{\mu\nu}^{\downarrow\uparrow} & M_{\mu\nu}^{\downarrow\downarrow} \end{pmatrix} = \begin{pmatrix} \langle \psi_{\mu\uparrow}^T | U_{T\uparrow\uparrow} | \psi_{\mu\uparrow}^{S,loc} \rangle \cos(\theta/2) & -\langle \psi_{\mu\uparrow}^T | U_{T\uparrow\uparrow} | \psi_{\mu\downarrow}^{S,loc} \rangle \sin(\theta/2) \\ \langle \psi_{\mu\downarrow}^T | U_{T\downarrow\downarrow} | \psi_{\mu\uparrow}^{S,loc} \rangle \sin(\theta/2) & \langle \psi_{\mu\downarrow}^T | U_{T\downarrow\downarrow} | \psi_{\mu\downarrow}^{S,loc} \rangle \cos(\theta/2) \end{pmatrix} \quad (64)$$

$$= -\frac{2\pi\hbar^2}{m} \begin{pmatrix} \frac{C_\uparrow}{\varkappa_\uparrow} \psi_{\mu\uparrow}^{S,loc}(\vec{R}_T) \cos(\theta/2) & -\frac{C_\uparrow}{\varkappa_\uparrow} \psi_{\mu\downarrow}^{S,loc}(\vec{R}_T) \sin(\theta/2) \\ \frac{C_\downarrow}{\varkappa_\downarrow} \psi_{\mu\uparrow}^{S,loc}(\vec{R}_T) \sin(\theta/2) & \frac{C_\downarrow}{\varkappa_\downarrow} \psi_{\mu\downarrow}^{S,loc}(\vec{R}_T) \cos(\theta/2) \end{pmatrix} \quad (65)$$

In the last equation we followed the TH model to extract the tunneling matrix elements by replacing the wave function at the tip apex atom by a spherically symmetric *s*-wave. Also the Chen's rule for arbitrary orbitals can be followed in the spin-polarized case. In the following we assume that the spin-up and spin-down *s*-wave states can be characterized by the same decay constant \varkappa and the same normalization coefficient C , i.e. $\varkappa_\sigma = \varkappa$ and $C_\sigma = C$.

The tunneling current in the spin-polarized case becomes

$$I(\theta, V) = \frac{2\pi e}{\hbar} \sum_{\sigma\sigma'} \int_0^{eV} d\epsilon [f(E_F^T - eV + \epsilon) - f(E_F^S + \epsilon)] \quad (66)$$

$$\times n_{\sigma'}^T(E_F^T - eV + \epsilon) n_\sigma^S(E_F^S + \epsilon) |M_{\sigma\sigma'}(\theta, E_F^S + \epsilon, E_F^T - eV + \epsilon)|^2$$

In the TH model, the tunneling current simplifies to

$$I(\vec{R}_T, \theta, V) = \frac{16\pi^3 C^2 \hbar^3 e}{\varkappa^2 m^2} \int_0^{eV} d\epsilon [f(E_F^T - eV + \epsilon) - f(E_F^S + \epsilon)] \quad (67)$$

$$\times \left(n^T(E_F^T - eV + \epsilon) n^S(\vec{R}_T, E_F^S + \epsilon) + \vec{m}^T(E_F^T - eV + \epsilon) \cdot \vec{m}^S(\vec{R}_T, E_F^S + \epsilon) \right)$$

where n is the total charge density of states ($n = n_\uparrow + n_\downarrow$) of the tip or sample while \vec{m} is the magnetization vector, i.e. the corresponding "magnetic" density of states. A further approximations can be made by considering the tip to be characterized by an *s*-wave function. That allows to consider n^T to be a constant:

$$I(\vec{R}_T, \theta, V) = \frac{16\pi^3 C^2 \hbar^3 e}{\varkappa^2 m^2} \underbrace{(n^T N^S(\vec{R}_T, V))}_{\text{nonspin-polarized}} + \underbrace{\vec{m}^T \cdot \vec{M}^S(\vec{R}_T, V)}_{\text{spin-polarized}}, \quad (68)$$

where N^s and M^s are respectively the energy integrated charge-density and magnetization of the sample's atom at the tip location \vec{R}_T . The previous equation, widely used to interpret SP-STM, shows that the tunneling current can be decomposed into a non spin-polarized and spin-polarized contributions. In case of a non spin-polarized STM experiment, i.e., using either a nonmagnetic tip or sample, the second term vanishes and the current reduces to the classical result of the TH model. Furthermore, depending on the angle between the magnetization vectors of tip and sample, the current will change.

For completeness we give the corresponding differential conductivity in the spin-polarized case

$$\frac{dI}{dV}(\vec{R}_T, \theta, V) \propto \underbrace{(n^T n^S(\vec{R}_T, E_F + eV))}_{\text{nonspin-polarized}} + \underbrace{\vec{m}^T \cdot \vec{m}^S(\vec{R}_T, E_F + eV)}_{\text{spin-polarized}}. \quad (69)$$

Tunneling anisotropic magneto-resistance (TAMR)

We derived previously the tunneling current and the differential conductivity in case of a spin-polarized tip. If the tip is non spin-polarized, the current depends solely on the non spin-polarized part. Assume that the sample magnetization is oriented along the out-of-plane direction, and that one applies a magnetic field to reorient the magnetization to be in-plane. In some cases, for instance if SOC is present, this reorientation could affect the electronic structure [56]. In other words, this means that n^S then exhibits a dependence on the magnetization's orientation.

This can be noticed by considering the SOC potential

$$\hat{V}_{SOC} = \zeta \vec{L} \cdot \vec{S} = \zeta \begin{pmatrix} V_{SOC}^{\uparrow\uparrow} & V_{SOC}^{\uparrow\downarrow} \\ V_{SOC}^{\downarrow\uparrow} & V_{SOC}^{\downarrow\downarrow} \end{pmatrix} \quad (70)$$

where ζ is the SOC strength, \vec{L} and \vec{S} are the orbital and angular momenta. The Hamiltonian without SOC, H^0 , is spin-diagonal and the unperturbed Bloch eigenfunctions are $(\psi_{\vec{k}\mu\uparrow}^{(0)}, 0)^T$ and $(0, \psi_{\vec{k}\mu\downarrow}^{(0)})^T$. The Schrödinger equation for the perturbed wave function then reads

$$\begin{pmatrix} H^{0\uparrow} + V_{SOC}^{\uparrow\uparrow} - E & V_{SOC}^{\uparrow\downarrow} \\ V_{SOC}^{\downarrow\uparrow} & H^{0\downarrow} + V_{SOC}^{\downarrow\downarrow} - E \end{pmatrix} \begin{pmatrix} \psi_{\vec{k}\mu\sigma\uparrow} \\ \psi_{\vec{k}\mu\sigma\downarrow} \end{pmatrix} = 0. \quad (71)$$

The potential terms $V_{SOC\uparrow\downarrow}$ and $V_{SOC\downarrow\uparrow}$ are responsible for flipping the spin. Solving this equation for the minority-spin channel, i.e. $\sigma = \downarrow$, leads for the two components of the spinor in first-order perturbation theory:

$$\psi_{\vec{k}\mu\downarrow\uparrow}^{(1)} = \sum_{\nu} \frac{\langle \psi_{\vec{k}\nu\downarrow}^{(0)} | V_{SOC\downarrow\uparrow} | \psi_{\vec{k}\mu\uparrow}^{(0)} \rangle}{E_{\vec{k}\mu}^{0\uparrow} - E_{\vec{k}\nu}^{0\downarrow}} \psi_{\vec{k}\nu\downarrow}^{(0)} \quad (72)$$

and

$$\psi_{\vec{k}\mu\downarrow\downarrow}^{(1)} = \psi_{\vec{k}\mu\downarrow}^{(0)} + \sum_{\nu \neq \mu} \frac{\langle \psi_{\vec{k}\nu\downarrow}^{(0)} | V_{SOC\downarrow\downarrow} | \psi_{\vec{k}\mu\downarrow}^{(0)} \rangle}{E_{\vec{k}\mu}^{0\downarrow} - E_{\vec{k}\nu}^{0\downarrow}} \psi_{\vec{k}\nu\downarrow}^{(0)} \quad (73)$$

where the index (1) stands for the first-order solution and $E_{\vec{k}\mu}^{0\uparrow}$ the eigenenergy of the state $\psi_{\vec{k}\mu\uparrow}^0$. Since the DOS is related to $|\psi^{(1)}|^2$, it is expected that the DOS will change because of SOC in

a quadratic fashion: $\sim \sum_{\sigma\sigma'} (V_{SOC}^{\sigma\sigma'})^2$ but the denominator of the previous equations will play an important role. Indeed if the weight of the states close to those \vec{k} where the unperturbed spin-dependent bands cross, i.e. $E_{\vec{k}\mu}^{0\sigma} = E_{\vec{k}\mu}^{0\sigma'}$ the denominator becomes small and the bands strongly couple and the modification of the charge can be important.

To illustrate the dependence of the DOS on the SOC and rotation angle of the magnetization, we introduce a simple toy model initially proposed by Néel *et al.* [54, 62] that shows how the total DOS, and by that the tunneling current and differential conductivity, can be affected by the magnetization orientation.

Assume that in the energy window of interest, we have two states, say d_{z^2} and d_{zx} states, in the minority spin-channel originally located at energies ϵ_1 and ϵ_2 . For simplification, we consider full spin-polarization, meaning that no orbitals are present in the majority spin channel. The hybridization with the background is described via Γ_1 and Γ_2 . The interaction between the two terms is provided via a hopping term t which in our case is created by SOC. The form of t is inferred from the work of Abate and Asdente [63] on bulk Fe who used a tight-binding formalism to evaluate the matrix elements $|\langle d_m | V_{SOC} | d_{m'} \rangle|$.

The matrix element connecting our orbitals are given by

$$|\langle d_{zx} | V_{SOC} | d_{z^2} \rangle| = \frac{1}{2} \sqrt{3} \zeta \sin \theta \sin \phi \quad (74)$$

for the minority spin-channel. θ and ϕ are the Euler angles defining the orientation of the magnetization.

We calculate the density state of this two-orbitals model by evaluating the Green function $G = (1 - H)^{-1}$ from which the imaginary part is extracted ($n(E) = -\frac{1}{\pi} \sum_{m=1}^2 \Im G_{mm}(E)$). We find

$$\hat{G} = \frac{1}{(E - \epsilon_1 - i\Gamma_1)(E - \epsilon_2 - i\Gamma_2) - t^2} \begin{pmatrix} E - \epsilon_1 - i\Gamma_1 & t \\ t & E - \epsilon_2 - i\Gamma_2 \end{pmatrix}, \quad (75)$$

where one notices that the diagonal elements of the Green functions, G_{mm} are proportional to t^2 , i.e., to V_{soc}^2 which bears the angular dependence. Thus this toy model indicates, that in the presence of SOC, the local DOS will depend on the orientation angle of the magnetization vector. The results obtained with $\zeta = 50$ meV (approximate value for $3d$ transition elements) are depicted in Fig. 6(a) where the corresponding DOS is shown for two different orientations, out-of-plane ($\theta = 0^\circ$) and in-plane ($\theta = 90^\circ, \phi = 0^\circ$). One notices that changes occur for both orbitals upon rotation. From our different formulas giving the tunneling current it is obvious that since the charge of the sample gets modified, the current magnitude will be affected by the rotation of the magnetization vector. In Fig. 6(b) is presented the corresponding TAMR signal, given by $\frac{n(\theta=0) - n(\theta=90)}{n(\theta=0)}$. A value of 20% is found at the position of the d -resonances where the large change in the DOS is observed. Experimentally, it is thus worthwhile to probe the sample at those energies where the largest TAMR effect is observed. It is interesting to check the angle dependence of the DOS as shown in Fig. 6(c). Interestingly, the d_z^2 contribution to the DOS, thus the tunneling current, versus the rotation angle follows a \sin^2 behavior in contrast to the cosine behavior of the spin-polarized part of the tunneling current in the SP-STM geometry when SOC is not included.

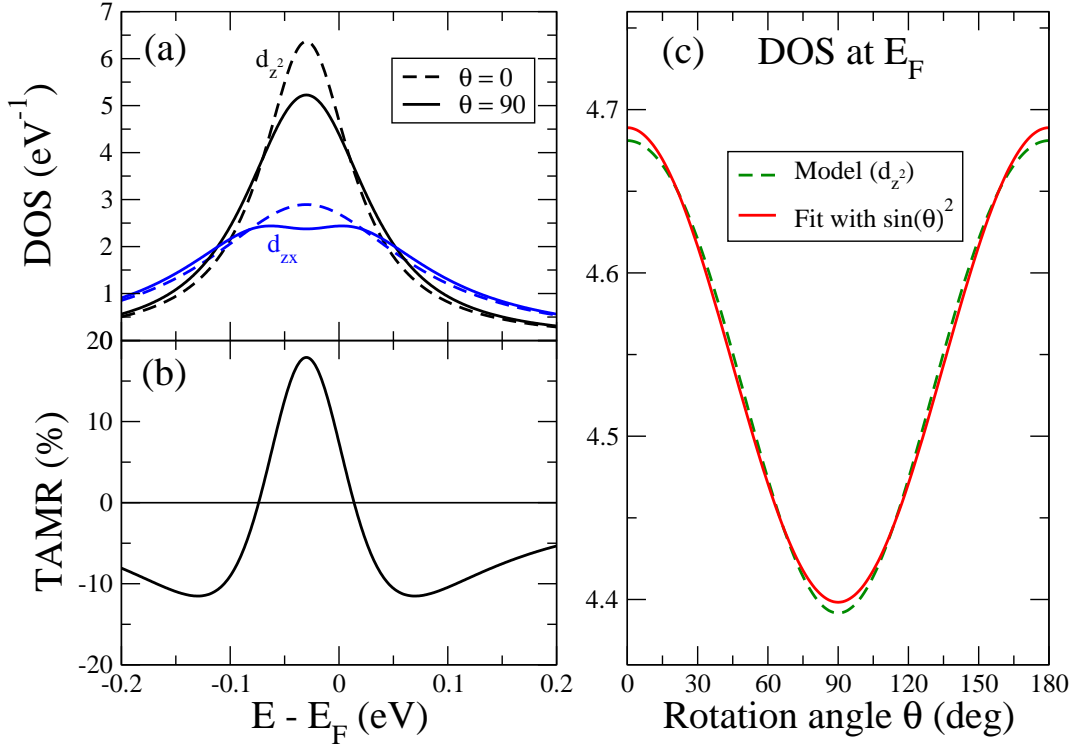


Fig. 6: (a) DOS obtained from a simple model for two d orbitals interaction via SOC (see Refs.[54, 62]). Dashed and full lines refer to the DOS calculated when the magnetization is out-of-plane and in-plane. The corresponding TAMR signal is plotted in (b) while the variation of the d_{z^2} -DOS at E_F with respect to the rotation angle θ is shown in (c).

4.5 Crystal surfaces: k_{\parallel} -Selection in STM

The DOS in vacuum above the substrate can be computed with ab-initio method, but for bulk systems before getting the DOS in real space a summation over k -points in reciprocal space has to be performed within the Brillouin zone. It is instructive to realize that not all k -points contribute equally to the vacuum's DOS. Indeed on a surface probed by STM, because of symmetry reduction only the parallel component, \vec{k}_{\parallel} , of the the three dimensional Bloch vector $\vec{k} = (k_{\perp}, \vec{k}_{\parallel})$ remains as a good quantum number. Thus in vacuum the wave function, $\psi_{\vec{k}_{\parallel}\mu}$, describing the surface characterized on the basis of Bloch theorem by a band index μ and a wave-vector \vec{k}_{\parallel} of the two-dimensional (2D) Brillouin zone is expanded into basis functions:

$$\psi_{\vec{k}_{\parallel}\mu}(\vec{r}_{\parallel}, z) = \sum_{\alpha} c_{\vec{k}_{\parallel}\mu}^{\alpha} d_{\vec{k}_{\parallel}\mu}^{\alpha}(z) \exp [i(\vec{k}_{\parallel} + \vec{G}_{\parallel}^n)\vec{r}_{\parallel}] \quad (76)$$

which are 2D plane waves parallel to the surface. \vec{G}_{\parallel}^n denotes the reciprocal lattice vectors parallel to the surface while $d_{\vec{k}_{\parallel}\mu}^{\alpha}$ are basis functions describing the decay of the substrate's states into vacuum and can be obtained by solving the one-dimensional Schrödinger equation

in vacuum

$$\left(-\frac{\hbar^2}{2m} \frac{d^2}{dz^2} + U(z) - \epsilon_\mu + \frac{\hbar^2}{2m} (\vec{k}_{||} + \vec{G}_{||}^\alpha)^2 \right) d_{\vec{k}_{||}}^\alpha(z) = 0, \quad (77)$$

for a given vacuum potential $U(z)$ and reference energy ϵ_μ .

In general, quantities possessing the crystal symmetry of the lattice can be expanded into a set of symmetrized functions. The local density of states (LDOS)

$$\begin{aligned} n(\vec{r}_{||}, z; \epsilon) &= \sum_{\vec{k}_{||\mu}} \delta(\epsilon - \epsilon_{\vec{k}_{||\mu}}) |\psi_{\vec{k}_{||\mu}}(\vec{r}_{||}, z)|^2 \\ &= \sum_{\vec{k}_{||\mu}} \delta(\epsilon - \epsilon_{\vec{k}_{||\mu}}) \sum_{\beta} n_{\vec{k}_{||\mu}}^\beta(z) \exp(i\vec{G}_{||}^{\beta} \vec{r}_{||}) \end{aligned} \quad (78)$$

where $\exp(i\vec{G}_{||}^{\beta} \vec{r}_{||})$ are called star coefficients and

$$n_{\vec{k}_{||\mu}}^\beta(z) = \sum_{\alpha\alpha'} c_{\vec{k}_{||\mu}}^\alpha c_{\vec{k}_{||\mu}}^{\alpha'*} d_{\vec{k}_{||\mu}}^\alpha(z) d_{\vec{k}_{||\mu}}^{\alpha'*}(z) \delta(\vec{G}_{||}^\alpha - \vec{G}_{||}^{\alpha'}, \vec{G}_{||}^\beta) \quad (79)$$

d could be the s -orbital as proposed in TH model, or one can use arbitrary orbitals according to the derivative rule of Chen.

One could grasp the behavior of the LDOS in vacuum by considering for simplicity that $U(z) = 0$. Thus the exact solution of the one dimensional Schrödinger equation in vacuum gives $d_{\vec{k}_{||}}^\alpha = \exp(-\varkappa_{\vec{k}_{||}}^\alpha z)$ where $z > 0$. The decay constant

$$\varkappa_{\vec{k}_{||}}^\alpha = \sqrt{2m|\epsilon_\mu|/\hbar^2 + (\vec{k}_{||} + \vec{G}_{||}^\alpha)^2} \quad (80)$$

and the related LDOS

$$n_{\vec{k}_{||\mu}}^\beta(z) = \sum_{\alpha\alpha'} c_{\vec{k}_{||\mu}}^\alpha c_{\vec{k}_{||\mu}}^{\alpha'*} \exp[-(\varkappa_{\vec{k}_{||\mu}}^\alpha + \varkappa_{\vec{k}_{||\mu}}^{\alpha'})z] \delta(\vec{G}_{||}^\alpha - \vec{G}_{||}^{\alpha'}, \vec{G}_{||}^\beta) \quad (81)$$

show obviously a strong dependence on $\vec{k}_{||}$ and on $\vec{G}_{||}^\alpha$.

The last equations demonstrate that the decay constant is the largest and thereby the LDOS is the smallest when contributions of $|\vec{k}_{||} + \vec{G}_{||}^\alpha|$ are significant. A decrease in \varkappa of 0.1 \AA^{-1} could lead to a reduction of the LDOS and of the tunneling current of the order of 50%.

Also the nature of the lattice can affect tunneling, as demonstrated in the following example. We show the first three vectors responding to the smallest “stars” ($m=1, 2, 3$) of reciprocal lattice vectors of a square lattice (see Fig. 7), which would represent the bcc(001) or fcc(001) surfaces. The corresponding reciprocal lattice vectors are $\vec{G}_{||}^{(1)} = (0, 0)$, $\vec{G}_{||}^{(2)} = (1, 0)$, and $\vec{G}_{||}^{(3)} = (1, 1)$, expressed in units of $2\pi/a$, with a being the lattice constant and the star coefficients are:

$$\exp(i\vec{G}_{||}^{(1)} \vec{r}_{||}) = 1 \quad (82)$$

$$\exp(i\vec{G}_{||}^{(2)} \vec{r}_{||}) = \frac{1}{2} [\cos(\vec{G}_{||,1} \vec{r}_{||}) + \cos(\vec{G}_{||,2} \vec{r}_{||})] \quad (83)$$

$$\exp(i\vec{G}_{||}^{(3)} \vec{r}_{||}) = \cos[(\vec{G}_{||,1} + \vec{G}_{||,2}) \vec{r}_{||}]. \quad (84)$$

$\vec{G}_{||,1} = \frac{2\pi}{a}(1, 0)$ and $\vec{G}_{||,2} = \frac{2\pi}{a}(0, 1)$ are the two-dimensional reciprocal lattice vectors. In Fig. 7 the star functions are displayed together with the 2D unit cell for a checkerboard structure

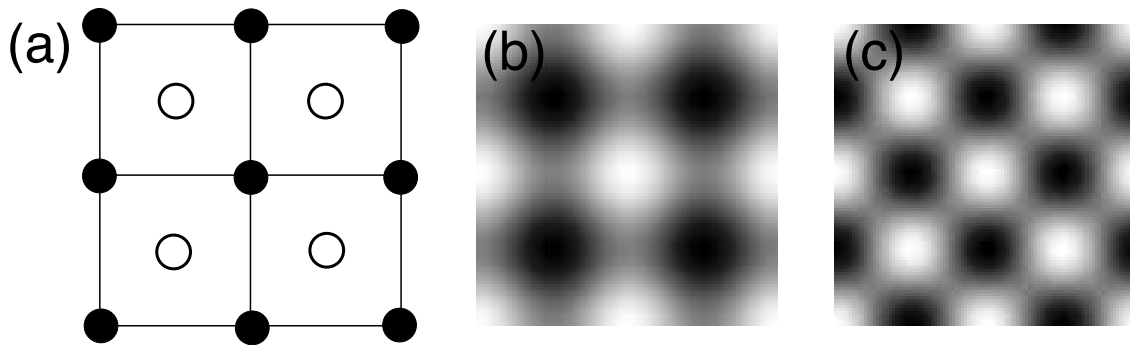


Fig. 7: Star functions for a square lattice according to Ref. [38]. (a) unit cell of a square lattice with a two-atoms basis, i.e. representing a checkerboard structure. The first star function is a constant contrary to the second one which leads to a chemical sensitivity on the two atoms (b). The black atoms are displayed as protrusions and the white ones as depressions. Interestingly the third star function shows equally both atoms (c).

with two different atom types. The first star function is a constant and represents the lateral constant part of the LDOS and thereby also of the tunneling current in the TH-model. Higher star coefficients can contribute non-trivially to the final STM image. The second coefficient for example, allows to distinguish between the two kinds of atoms while the third coefficient does not, i.e., chemical sensitivity is probed only by the second star coefficient.

Any magnetic superstructure lowers the translational symmetry. Therefore, smaller reciprocal lattice vectors become relevant for the spin-polarized part of the tunneling current with coefficients that are consequently exponentially larger than those of the unpolarized part.

5 Examples of simulations and experiments

5.1 Seeing the Fermi surface in real space via the induced charge oscillations

Friedel oscillations define an important concept in quantum mechanics. They are created after perturbing an electron gas with an impurity. Charge and magnetic oscillations are then obtained in the surrounding electron gas. The shape and intensity of these oscillations contain important information on the impurity's electronic structure and on the band-structure of the host material where the impurity is embedded. As mentioned earlier, STM allowed to observe Friedel oscillations induced on surfaces characterized by two-dimensional electronic surface states. These surfaces, typically, Cu(111), Ag(111) and Au(111) surfaces provided the right playground for experimental and theoretical investigations on charge variations induced by impurities in a quasi-two-dimensional electron gas.

Isotropic Friedel oscillations

For Cu(111) the surface state shows a parabolic dispersion with a minimum at ~ 0.5 eV below the Fermi level. The corresponding band structure projected on the $\bar{\Gamma} - \bar{M}$ line of the

2D-Brillouin zone is shown in Fig. 8(a). The shaded regions indicate the regions in $E - k_{\parallel}$ space, for which bulk eigenstates (Bloch waves) exist. Surface states can only exist in the white "gap"-regions. Two such states are indicated. Of special interest is the parabolic band with the minimum close to E_F , since this state is only partially occupied and gives rise to a two-dimensional metallic behavior, which is of great interest for the following.

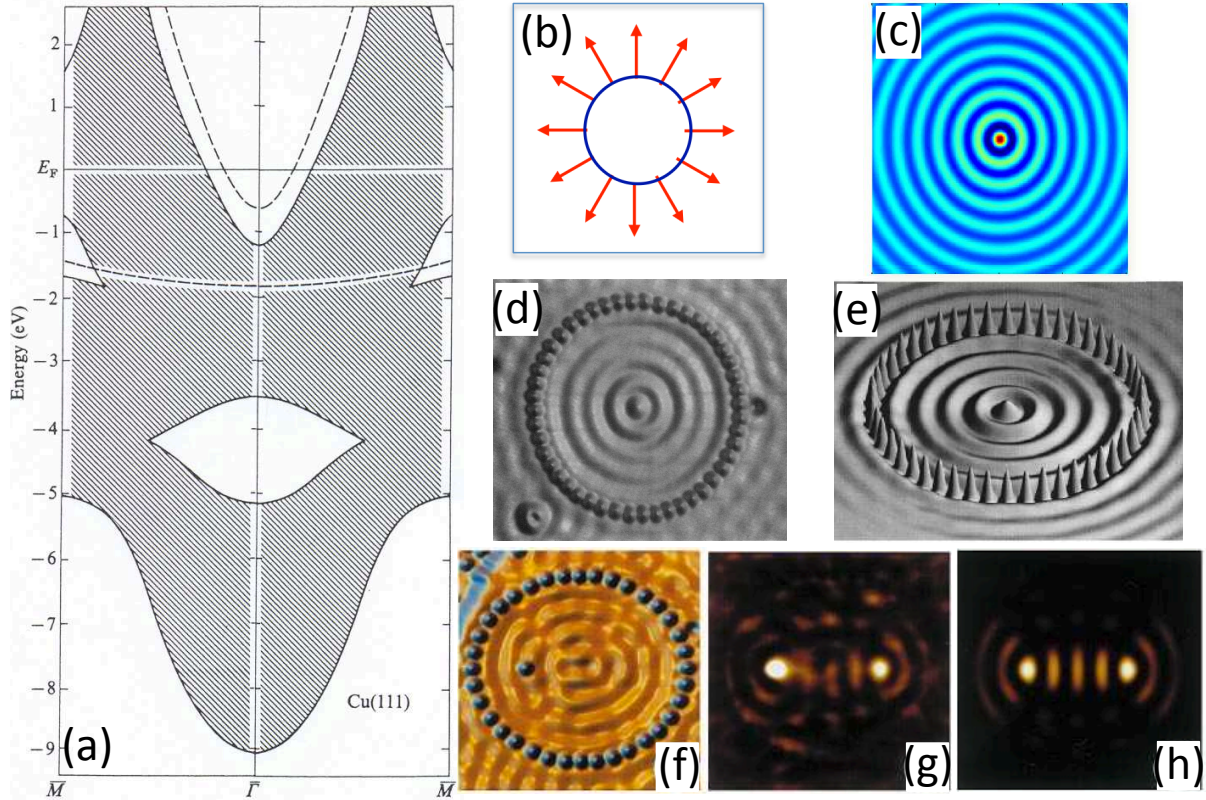


Fig. 8: (a) Surface states (dashed curves) and bulk projected bands at a Cu(111) surface according to a six-layer surface band structure calculation [64]. In (b) and (c) illustration of the relation between the isotropic shape of the Fermi surface (black contours), group velocities (red arrows) in (b) and the corresponding induced isotropic charge oscillations in (c). In (d) and (e) is shown a comparison between the tunneling spectra obtained for a corral of Fe adatoms on Cu(111) surface as measured by Crommie et al. [5] (d) to the calculations made with the KKR method [65](e). Visualization of the quantum mirage with a mirage effect is shown in (f), (g) and (h). (f) is a topography showing an ellipse with $e = \frac{1}{2}$ and a Co atom at the left focus. In (g) the associated $\frac{dI}{dV}$ difference map shows the Kondo effect projected to the empty right focus, resulting in a Co atom mirage. This experimental measurement compares well with the calculated eigenmodes at E_F (magnitude of the wave function is plotted) as shown in (h). [7]

For defects in the bulk, these Friedel oscillations of the charge perturbation vary for large distances r as $1/r^3$ times an oscillatory function and are in the jellium model proportional to:

$$\Delta n(r) \sim \frac{\cos(2k_F r + \delta)}{r^3} \quad (85)$$

However in the case of adatoms on surfaces, the charge response decays for long in-plane distances r slower than in the bulk and is determined by the surface states. In a free electron model, being well suited for the above surface state for Cu(111), the charge density is for large distances r proportional to

$$\Delta n(r) \sim \frac{\sin(2k_F r + \delta)}{r^2} \quad (86)$$

However, since also bulk states exist, which span most of the phase space (see Fig. 8(a)), the short range screening of the defect is dominated by these states, while only the long ranged behavior is determined by the surface state, which has a small wave vector k_F leading to long wave length oscillations.

In Fig. 8(b) and (c), are shown the Fermi surface of a two-dimensional electron gas with group velocities (vectors shown in red) and the corresponding induced charge around the impurity which is then isotropic and circular. The shape of the induced oscillations indicate that the related energy contour in reciprocal space is circular.

Many authors have observed such long ranged oscillations around adatoms, small clusters and steps on the Cu(111) surface in STM experiments. Most prominent among these is the work of the team of Eigler *et al.* [4, 5, 6, 7]. By atomic manipulations they were able to construct a corral of Fe atoms on the (111) Cu surface, and have shown that the surface states in the corral are more or less localized and form a discrete spectrum of resonant states. As an illustration of these we show in Fig. 8(d) and (e) a comparison of the experimental measurements to the result of calculations of Crampin *et al.* [65] obtained with the Korringa-Kohn-Rostoker Green function (KKR) method for a circular corral of 48 Fe atoms on the Cu(111) surface. Shown are the local density of states at the Fermi energy at 5 Å above the surface. Within the corral one sees a quantum well state with five maxima, corresponding to a localized state being more or less completely confined to the corral. Outside one sees oscillations arising from scattered surface state electrons at the corral, which decay with distance.

Let us shortly discuss the reason for the strong scattering of the surface state electrons at the Fe atoms. Basically in the vacuum region the full potential of Fe acts as a scattering center for the surface wave, being much stronger than the scattering at an Fe impurity in the bulk, where only the change of the Fe potential with respect to the host potential is effective. Moreover the wave vector k_F is relatively small, such that the wave length is considerably larger than the spacing between the Fe atoms. Therefore the surface wave does not “see” the corrugation of the Fe ring and is strongly reflected as in a cylindrical well. In fact the sequence of resonances can be well described by such a quantum well model, as has been shown recently [66]. The most fascinating corral experiments are the observation of atomic mirages in an elliptical quantum well [7]. An ellipse has the well known property that all classical waves emanating from one of the two focus points in every direction are reflected from the ellipse wall and focused in the second point, where these waves add up coherently since each such partial wave has the same path length and therefore the same phase shift. This is illustrated in Figs. 8(f–h) taken from Ref. [7]. Fig. 8(f) shows the STM topography for an ellipse with a given eccentricity, including one Co atom at the left focus point. Fig. 8(g) shows the $\frac{dI}{dV}$ difference maps, i.e. the change of the STM intensity map with respect to a small bias voltage V , which corresponds in the calculations to the local density of states in the vacuum region at the height of the STM tip. We see clearly two intensity spots, the real Co atom at the left focus and its image at the right focus. Thus in the empty focus we see the same accumulation of charge in the surface state as around the Co atom; therefore the image is called a quantum mirage. In fact the Co atom is a Kondo impurity

and a strong and sharp Kondo peak appears only in a very small energy region of about 10 meV around the Fermi level. Moreover the large mirage only appears, if one of the quantum well states falls into this energy region. Fig. 8(h) shows the calculated localized eigenstate observed in the experiment. The calculated local density of states compares very well with the $\frac{dI}{dV}$ curve shown in Fig. 8(h). Thus several conditions have to be satisfied for the Co mirage to appear: (i) the Co-atom has to sit in a focus point; if it sits at another position away from the focus point, no image appears, (ii) the bias voltage has to be such, that it coincides with an eigenstate of the ellipsoidal corral having maxima at the focus points, (iii) finally the image is particularly intense, if the eigenvalue coincides with the Kondo resonance. This concept has been recently extended theoretically by Stepanyuk and co-workers for the induced magnetization confined in magnetic corrals [67].

Focusing effect

If one manages to embed a Co-impurity few layers underneath the surface and try to visualize the induced Friedel oscillations on the surface, strange patterns are observed. Recently, we have shown by ab-initio calculations combined with STM observations that anisotropic localized oscillations can be observed on top of Cu(111) and Cu(001) surfaces due to the presence of buried Co impurities [68, 69]. These anisotropic ripples show that the usual isotropic free-electron model is not valid in such real situations. We demonstrated that these intriguing features are nothing else than a visualization in real space of parts of the bulk copper Fermi surface that are relatively flat. For the comparison between theory and STM, use is made of the Tersoff-Hamann model stating, as mentioned earlier, that scanning tunneling spectra can be related to the DOS in a certain energy interval in the vacuum.

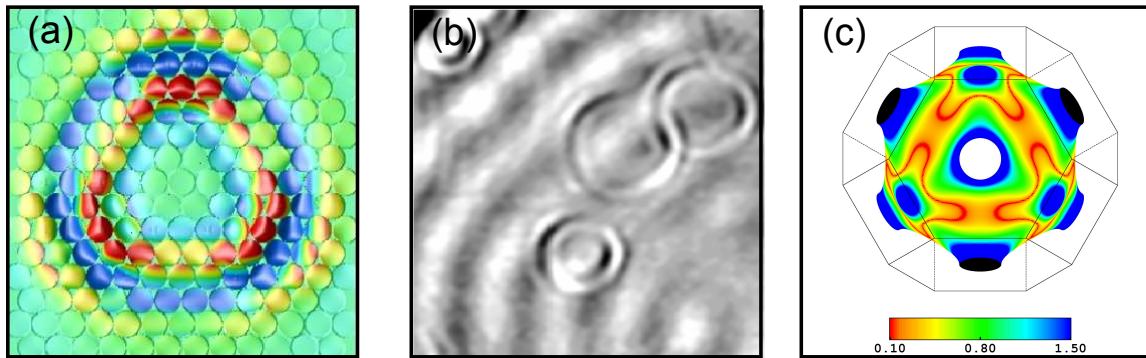


Fig. 9: (a) Impurity induced charge density around E_F for an area of $\approx 30 \times 30 \text{ \AA}^2$ calculated at a height $\approx 6.1 \text{ \AA}$ above the Cu(111) surface with a Co impurity sitting in the 6th layer below the surface. (b) Experimental STM topographies for an area of $90 \times 90 \text{ \AA}^2$ (-80mV , 1nA) of four Co atoms below the Cu(111) surface. (c) Fermi surface of copper represented along the (111) direction. The inverse mass tensor corresponding to the denominator of Eq. 88 is represented by the color in units of the inverse electron mass. Small values represented in red lead to high intensities of the charge variation.

Fig. 9(a) shows an example of the results of our simulations: the case of a Co impurity sitting

at the 6th layer below the Cu(111) surface (-12.5Å below the surface). The charge induced in the vacuum has been computed up to an area of $30 \times 30 \text{ \AA}^2$ above the impurity. One notices the triangular shape of the induced charge with high values at the corners of the triangle. In addition, a one and a half period ripple can be observed to oscillate from the red positive value to the blue negative values and finally to the almost zero green values. The same period was also noticed in the STM experiment (Fig. 9(b)). To understand such a phenomenon, we start by giving the form of the induced variation of the DOS in the vacuum at position 0 by some buried Co impurity sitting at a position defined by \vec{R} and inducing a change in the potential ΔV :

$$\Delta n_{\text{vacuum}}(\epsilon) \sim -\frac{1}{\pi} \Im \left[\int \int d^3r d^3r' G_0(0, \vec{r}; \epsilon) \Delta V(\vec{r}') G_0(\vec{r}', 0; \epsilon) \right] \quad (87)$$

where the Green function, G_0 , obtained from the KKR method, describes the pure substrate. At very large distances R between the impurity and the vacuum site one can apply the stationary phase approximation and end up with a result similar to that of the well-known theory of interlayer exchange coupling:

$$R^2 \Delta n_{\text{vacuum}} \propto \frac{1}{\left| \frac{d^2 E}{dk_x^2} \cdot \frac{d^2 E}{dk_y^2} \right|}. \quad (88)$$

The denominator of this equation is a measure of the curvature of the constant energy surface, i.e., the shape of the constant energy surface affects the propagation of the electrons. Additionally, one can show that the electronic waves are directed by the group velocities. Since, states at the Fermi energy (E_F) are probed experimentally, the constant energy surface corresponds to the Fermi surface: a small value of the curvature means that the Fermi surface has a flat region leading to large values of the DOS and to strong focusing of intensity in this space region determined by the group velocity. In Fig. 9(c), we show the Fermi surface, computed with ab-initio, of Cu oriented with the (111)-neck direction normal to the drawing plane. The Fermi surface is colored following the strength of the denominator of the right hand side of Eq. 88. The shape of the low values of this denominator, corresponding to the flat regions of the Fermi surface is found to be rather triangular along the (111) direction in accordance with our simulations of the induced Friedel oscillations. One can understand that the flat region seen within the triangle in Figs. 9(a) and (b) is induced by the neck of the Cu Fermi surface along the (111) direction that does not allow electrons to propagate.

Once the shape of the propagator G is known, either by STM-investigation or calculations based on density functional theory many additional effects can be predicted. The strong directionality of electron propagation even for a simple metal such as Cu, has consequences in many fields. For example, the spatially anisotropic characteristics should also be equally present in the RKKY interactions between magnetic impurities. Indeed we have shown that the interaction between Co adatoms on Pt(111) surface or Fe adatoms on Cu(111) surface is very anisotropic [20, 21], which is obviously induced by the same physics discussed in this subsection, i.e. the anisotropic shape of the Fermi surface.

5.2 Magnetism on surfaces with SP-STM

An example calculated by Heinze and collaborators [27] is shown in Fig. 10(a) and (b). A Cr overlayer on Ag(111) shows a row-wise antiferromagnetic structure (actually the ground state calculated by the authors is non-collinear, but for now we focus on the antiferromagnetic state).

The row-wise antiferromagnetism is indicated by the arrows drawn at the atomic positions, showing the magnetization direction of each atom. A scan of the surface with a non-magnetic STM tip will show the chemical unit cell (Fig. 10(a)): bright spots correspond to the Cr atoms, from which a tunneling current flows to the tip when the apex atom is above them. But a scan with a spin polarized tip reveals the magnetic structure (Fig. 10(b)). Instead of bright spots appearing around each atom, now bright stripes emerge at the rows with a magnetization direction parallel to the one of the tip, while dark stripes appear at the rows with opposite magnetization.

In these calculations, the assumption of a fully spin-polarized tip was made: i.e. $n_{T\downarrow}(E_F) = 0$. In Figs. 10(a) and (b), we see that the bright stripes (high current) appear when the substrate magnetization is parallel to the one of the tip. It should be noted that this is by no means guaranteed for all cases; it can well be that the antiparallel orientation favors the tunneling current. Eventually a case might be encountered where the parallel and antiparallel configurations give an almost equal signal at E_F . In this case spectroscopy is a very valuable tool, since one can detect the signal at other energies, choosing a voltage for which the two spin directions give considerably different results.

Another example of comparison between experiment and theory is shown in Figs. 10(c) and (d) for the case of Mn overlayer on W(110) surface. This work, realized by Heinze *et al.* [9], was the first observation of antiferromagnetism in a single magnetic layer. They found, as in the precedent example, that nonspin-polarized tunneling electrons image the chemical surface unit cell without any magnetic contribution, whereas spin-polarized electrons probe the change in translational symmetry due to the magnetic superstructure, which gives rise to a different image corresponding to the respective magnetic structure. The magnetic ground state that is antiferromagnetic in a checkerboard arrangement of Mn atoms with magnetic moments of opposite direction and an easy axis of the magnetization oriented in the film plane leads in the theoretical STM image to a stripe pattern similar to the one obtained experimentally. However, when the STM tip is considered non-magnetic, all Mn atoms become equivalent in the chemical unit cell and the STM-pattern becomes diamond-like both experimentally and theoretically. A detailed discussion on magnetism and in particular on magnetism at surfaces is given in Chapter C 4 by S. Blügel.

5.3 Magnetic domain walls with TAMR-STM

The first experimental verification of the dependence of the DOS on the magnetization orientation was provided experimentally by Bode *et al.* [52] using a non spin-polarized STM on Fe double layers deposited on W(110) substrate. This effect discussed in Section 4.4, was already predicted theoretically [56]. The substrate chosen by Bode *et al.* is well known for having a nanometer-scale domain structure. In other words, the magnetization of the sample rotates at the nanometer-scale as shown in Fig. 11(a) and the idea is to probe the rotation of the magnetization at different positions using the spectroscopic mode, i.e. to measure the dI/dV spectra.

Interestingly, the domain walls are visible with a non-magnetic W tip (see Fig. 11(b)) along the different stripes propagating laterally: At the position of the domain wall the differential conductivity dI/dV is reduced with respect to the domain. As revealed by the local tunneling spectra (Fig. 11(c)), this contrast is caused by a tiny difference which is energetically located just above E_F (see inset): while the dI/dV spectrum measured with the tip positioned above the domain exhibits a weak peak at a bias of 0.07 eV, this peak is almost absent in the domain wall

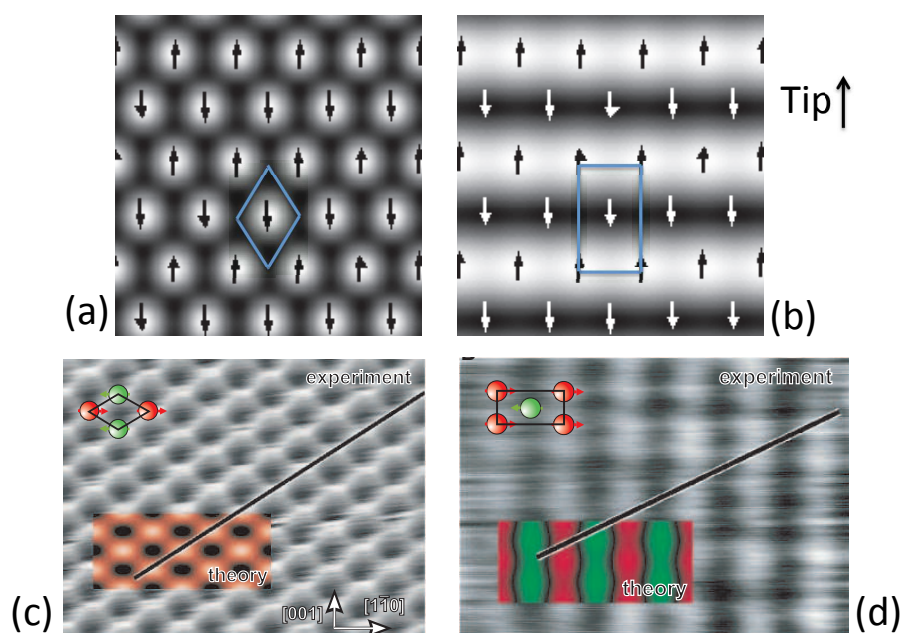


Fig. 10: Calculated STM picture of an antiferromagnetic Cr monolayer on Ag(111) fcc surface after Ref. [27] and Mn monolayer on W(110) surface after Ref. [9]. In (a) shows the result obtained assuming a non spin-polarized tip, revealing the chemical unit-cell (drawn parallelogram); Cr atoms appear as white filled circles. In (b) a spin-polarized tip with magnetization direction in-plane as indicated. In this case the magnetic unit cell emerges (drawn as a rectangle), giving alternating black and white stripes. The drawn arrows indicate the magnetization direction of each Cr atom. A comparison of SP-STM measurements and first-principles calculations for the case of Mn layer on W(110) is shown in (c) considering a non-magnetic tip and in (d) when the tip is magnetic. Once more the unit-cell of the calculated magnetic ground state is shown in the insets of (c) and (d).

spectra. This is further illustrated in the lower part of Fig. 11(c) by the plot of the TAMR ratio calculated as $[(dI/dV)_D - (dI/dV)_W]/[(dI/dV)_D + (dI/dV)_W]$, where the dI/dV are taken within the domain (D) or at the domain wall (W).³ For comparison, first-principles calculations of the LDOS and TAMR ratio on the same system including SOC were performed considering different rotations (out-of-plane and in-plane) of the magnetic moments are shown in Fig. 11(d). The agreement is good and it is found theoretically that the two minority-spin d_{z^2} states at the Fe surface lead to pronounced peaks at -0.18 and +0.85 eV and can be identified with the experimental peaks at -0.08 eV and +0.7 eV. A closer look (cf. inset in Fig. 11(d)) reveals a significant enhancement of the LDOS for the out-of-plane magnetized film within an energy interval of about 100 meV above E_F . The theoretical TAMR signal is qualitatively in line

³If the ratio is calculated on the original data (as measured), a pronounced oscillation can be found just below E_F . This oscillation is not caused by any additional or missing spectroscopic features in the domain wall of the dI/dV spectrum with respect to the spectrum measured at domains but by an overall energetic shift ~ 11 meV. The physical origin is different work functions in domains and domain walls. After correction, the oscillation below E_F has almost perfectly disappeared.

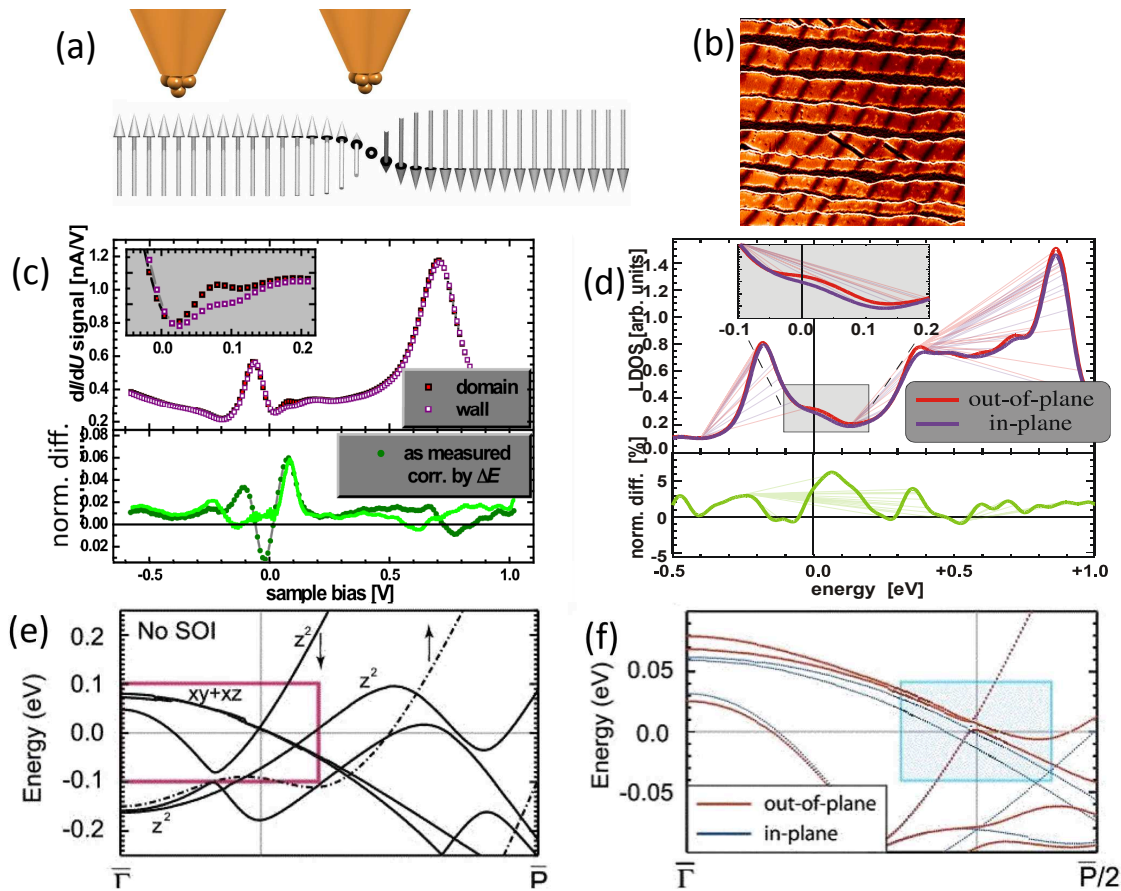


Fig. 11: (a) Measurement of a domain wall with an STM-probe at different location: within the domain and at the domain-wall. (b) shows an image of the dI/dV signal measured on two-monolayers Fe deposited on W(110) substrate. Stripes of ~ 50 nm widths can be observed with bright (within the domain \sim in-plane orientation of the magnetization) and dark (at the domain-wall \sim out-of-plane orientation of the magnetization) regions. In (c) and (d) are shown the bias-dependence of the dI/dV signal and the theoretical LDOS at different locations: domain (in-plane magnetization) and domain-wall (out-of-plane) regions. A TAMR ratio is computed and shown in lower parts of (c) and (d). The band-structure calculated without (e) and with SOC (f) demonstrates the impact of SOC and of the orientation of the magnetization on the electronic structure of the sample. Figures taken and adapted from Ref.[52]

with the experimental signal: The peak at -0.3 eV could be identified with the experimental peak at -0.24 eV. The origin of the dependence of the LDOS on SOC can be traced back to the change of the band-structure once the magnetization is rotated as discussed in Section 4.4. The band-structure without and with SOC are plotted in Figs. 11(e) and (f). States at the $\bar{\Gamma}$ point decay the lowest into vacuum (as discussed in Section 4.5). Around -0.18 eV and $+0.05$ eV, the d_{z^2} -band crosses the $\bar{\Gamma}$ -point. Because of their appropriate extension in the z -direction, the d_{z^2} orbitals decay slower into the vacuum compared to the d_{xz} and d_{yz} orbitals. Interestingly, the crossing of the minority d bands that occurred without SOC is avoided once SOC is included

and if the magnetization is rotated out-of-plane (red line in Fig. 11(f)). This has a strong impact by shifting, for example, the crossing of the bands at the $\bar{\Gamma}$ -point. Overall such a small effect is enough to induce a change in the LDOS that is observable with STM. We note that the use of TAMR within STM was recently extended to probe adatoms deposited on surfaces with magnetic domain walls [54, 55].

Acknowledgment

I would like to acknowledge the HGF-YIG Programme VH-NG-717 (Functional Nanoscale Structure and Probe Simulation Laboratory–Funsilab) for financial support.

References

- [1] G. Binnig, H. Rohrer, Ch. Gerber and E. Weibel, *Appl. Phys. Lett.* **40**, 178 (1982).
- [2] G. Binnig, H. Rohrer, Ch. Gerber and E. Weibel, *Phys. Rev. Lett.* **49**, 57 (1982).
- [3] G. Binnig, H. Rohrer, Ch. Gerber and E. Weibel, *Phys. Rev. Lett.* **50**, 120 (1983).
- [4] D. M. Eigler and E. K. Schweizer, *Nature* **344**, 524 (1990).
- [5] M. F. Crommie, C. P. Lutz, and D. M. Eigler, *Science* **262**, 218 (1993).
- [6] E. J. Heller, M. F. Crommie, C. P. Lutz and D. M. Eigler, *Nature* **369**, 466 (1994).
- [7] H. C. Manoharan, C. P. Lutz and D. M. Eigler, *Nature* **403**, 512 (2000).
- [8] R. Wiesendanger, H.-J. G'unterodt, G. G'unterodt, R. J. Gambino and R. Ruf, *Phys. Rev. Lett.* **65**, 247 (1990).
- [9] S. Heinze, M. Bode, A. Kubetzka, O. Pietzsch, X. Nie, S. Blügel and R. Wiesendanger, *Science* **288**, 1805 (2000).
- [10] S. Blügel, M. Weinert and P. H. Dederichs, *Phys. Rev. Lett.* **60**, 1077 (1988).
- [11] M. Bode, M. Heide, K. von Bergmann, P. Ferriani, S. Heinze, G. Bihlmayer, A. Kubetzka, O. Pietzsch, S. Blügel and R. Wiesendanger, *Nature* **447**, 190 (2007).
- [12] S. Loth, S. Baumann, C. P. Lutz, D. M. Eigler and A. J. Heinrich, *Science* **335**, 196 (2012).
- [13] S. Holzberger, T. Schuh, S. Blügel, S. Lounis and W. Wulfhchel, *Phys. Rev. Lett.* **110**, 157206 (2013).
- [14] B. C. Stipe, M. A. Razaee and W. Ho, *Science*, **279**, 5358 (1998).
- [15] A. J. Heinrich, J. A. Gupta, C. P. Lutz and D. M. Eigler, *Science* **306**, 5695 (2004).
- [16] C. F. Hirjibehedin, C. P. Lutz, A. J. Heinrich, *Science*, **312**, 5776 (2006).
- [17] T. Balashov, T. Schuh, A. F. Takács, A. Ernst, S. Osetanin, J. Henk, I. Merting, P. Bruno, T. Miyamachi, S. Suga and W. Wulfhchel, *Phys. Rev. Lett.* **102**, 257203 (2009).

- [18] A. A. Khajetoorians, S. Lounis, B. Chilian, A. T. Costa, L. Zhou, D. L. Mills, J. Wiebe and R. Wiesendanger, *Phys. Rev. Lett.* **106**, 037205 (2011).
- [19] S. W. Wu, N. Ogawa and W. Ho, *Science* **312**, 5778 (2003).
- [20] L. Zhou, J. Wiebe, S. Lounis, E. Vedmendenko, F. Meier, S. Blügel, P. H. Dederichs, R. Wiesendanger, *Nature Physics* **6**, 187 (2010).
- [21] A. A. Khajetoorians, J. Wiebe, B. Chilian, S. Lounis, S. Blügel, R. Wiesendanger, *Nature Physics* **8**, 497 (2012).
- [22] C.J. Chen, *Introduction to Scanning Tunneling Microscopy* (Oxford University Press, Oxford, 1993).
- [23] J. Tersoff and D.R. Hamann, *Phys. Rev. Lett.* **50**, 1998 (1983).
- [24] J. Tersoff and D.R. Hamann, *Phys. Rev. B* **31**, 805 (1985).
- [25] C.J. Chen, *Phys. Rev. B* **42**, 8841 (1990).
- [26] C. J. Chen, *Phys. Rev. Lett.* **65**, 448 (1990).
- [27] S. Heinze, P. Kurz, D. Wortmann, G. Bihlmayer, G. Bihlmayer and S. Blügel, *Appl. Phys. A* **75**, 25 (2002).
- [28] N. Lorente and M. Persson, *Phys. Rev. Lett.* **85**, 2997 (2000).
- [29] N. Lorente and J. P. Gauyacq, *Phys. Rev. Lett.* **103**, 176601 (2001).
- [30] M. Persson, *Phys. Rev. Lett.* **103**, 050801 (2009).
- [31] J. Fernandez-Rossier, *Phys. Rev. Lett.* **102**, 256802 (2009).
- [32] J. Fransson, *Nano Lett.* **9**, 2414 (2009).
- [33] A. Hurley, N. Baadji, and S. Sanvito, *Phys. Rev. B* **86**, 125411 (2012).
- [34] S. Lounis, A. T. Costa, R. B. Muniz and D. L. Mills, *Phys. Rev. Lett.* **105**, 187205 (2010).
- [35] S. Lounis, A. T. Costa, R. B. Muniz and D. L. Mills, *Phys. Rev. B* **83**, 035109 (2011).
- [36] H.-J. Günterodt and R. Wiesendanger (Ed.), *Scanning Tunneling Microscopy I–III*, (Springer, Heidelberg, 1994–1996).
- [37] R. Wiesendanger, *Scanning Probe Microscopy and Spectroscopy: Methods and Applications* (Cambridge University Press, Cambridge, 1994).
- [38] S. Heinze, *First-Principles Theory of Scanning Tunneling Microscopy Applied to Transition-Metal Surfaces*, PhD thesis, University of Hamburg (2000).
- [39] W. A. Hofer, A. S. Foster and A. L. Schluger, *Rev. Mod. Phys.* **75**, (2003).
- [40] M. Bode, *Rep. Prog. Phys.* **66**, 523 (2003).

- [41] R. Wiesendanger, *Rev. Mod. Phys.* **81**, 1495 (2009).
- [42] A. van Housel and H. J. W. Zandvliet, *Rev. Mod. Phys.* **82** 1593 (2010).
- [43] J. P. Gauyacq, N. Lorente and F. D. Novaes, *Prog. Surf. Sci.* **87**, 63 (2012).
- [44] S. Blügel, *Theorie der Rastertunnelmikroskopie*, in the lecture notes of the 30th IFF Spring School, Forschungszentrum Jülich (1999).
- [45] K. K. Saha, J. Henk, A. Ernst, and P. Bruno, *Phys. Rev. B* **77**, 085427 (2008).
- [46] C. F. Quate, *Vacuum Tunneling: A New Technique for Microscopy*, *Physics Today*, 26 (1986).
- [47] J. Bardeen, *Phys. Rev. Lett.* **6**, 57 (1961).
- [48] M. Jullière, *Physics Letters A*, **54** 225 (1975).
- [49] J. Slonczewski, *Phys. Rev. B*, **39**, 6995 (1989).
- [50] J. S. Moodera, L. R. Kinder, T. M. Wong and R. Meservey, *Phys. Rev. Lett.* **74**, 3273 (1995).
- [51] T. Yaoi, S. Ishio and T. Miyazaki, *J. Mag. Mag. Mat.* **126**, 430 (1993).
- [52] M. Bode, S. Heinze, A. Kubetzka, O. Pietzsch, X. Nie, G. Bihlmayer, S. Blügel and R. Wiesendanger, *Phys. Rev. Lett.* **89**, 237205 (2002).
- [53] C. Gould, C. Rüster, T. Jungwirth, E. Girgis, G. M. Schott, R. Giraud, K. Brunner, G. Schmidt and L. W. Molenkamp, *Phys. Rev. Lett.* **93**, 117203 (2004).
- [54] N. Néel, S. Schröder, N. Ruppelt, P. Ferriani, J. Kröger, R. Berndt and S. Heinze, *Phys. Rev. Lett.* **110**, 037202 (2013).
- [55] D. Serrate, P. Ferriani, Y. Yoshida, S-W. Hla, M. Menzel, K. von Bermann, S. Heinze, A. Kubetzka, R. Wiesendanger, *Nature Nanotechnology*, **5**, 350 (2010).
- [56] A. Lessard, T. H. Moos, and W. Hübner, *Phys. Rev. B* **56**, 2594 (1997).
- [57] T. Balashov, A. F. Takács, M. Däne, A. Ernst, P. Bruno, W. Wulfhekel, *Phys. Rev. B* **78**, 1774404 (2008).
- [58] S. Loth, M. Etzkorn, C. P. Lutz, D. M. Eigler, A. J. Heinrich, *Science* **329**, 5999 (2010).
- [59] A. A. Khajetoorians, B. Baxevanis, C. Hübner, T. Schlenk, S. Krause, T. O. Wehling, S. Lounis, A. Lichtenstein, D. Pfannkuche, J. Wiebe and R. Wiesendanger, *Science* **339**, 6115 (2013).
- [60] T. Miyamachi, T. Schuh, T. Markl, C. Bresch, T. Balashov, A. Stohr, C. Karlewski, S. Andre, M. Marthaler, M. Hoffmann, M. Geilhufe, S. Ostanin, W. Hergert, I. Mertig, G. Schon, A. Ernst and W. Wulfhekel, *Nature* **503**, 242 (2013).
- [61] D. Wortmann, S. Heinze, Ph. Kurz, G. Bihlmayer and S. Blügel, *Phys. Rev. Lett.* **86**, 4132 (2001).

-
- [62] S. Schröder, *First-Principles Study of Non-Collinear Magnetism and Spin-Orbit Driven Physics in Nanostructures at Surfaces*, PhD thesis, Christian-Albrechts University in Kiel (2013).
- [63] E. Abate and M. Asdente, *Phys. Rev. B* **140**, A1303 (1965).
- [64] A. Euceda, D. M. Bylander and L. Kleinman, *Phys. Rev. B* **28**, 528 (1983).
- [65] S. Crampin and O. R. Bryant, *Phys. Rev. B* **54**, 17367 (1996).
- [66] B. Lazarovits, B. Újfalussy, L. Szunyogh, B. L. Györffy and P. Weinberger, *J. Phys.: Condens. Matter* **17**, S1037 (2005).
- [67] V. S. Stepanyuk, L. Niebergall, W. Hergert and P. Bruno, *Phys. Rev. Lett.* **94**, 187201.
- [68] A. Weismann, M. Wenderoth, S. Lounis, P. Zahn, N. Quaas, R. G. Ulbrich, P. H. Dederichs and S. Blügel, *Science* **323**, 1190 (2009).
- [69] S. Lounis, P. Zahn, A. Weismann, M. Wenderoth, R. G. Ulbrich, I. Mertig, P. H. Dederichs and S. Blügel, *Phys. Rev. B* **83**, 035427 (2011).